

Analytical halo models of cosmic tidal fields

Aseem Paranjape^{1*}

¹ *Inter-University Centre for Astronomy & Astrophysics, Ganeshkhind, Post Bag 4, Pune 411007, India*

draft

ABSTRACT

The non-linear cosmic web environment of dark matter haloes plays a major role in shaping their growth and evolution, and potentially also affects the galaxies that reside in them. We develop an analytical (halo model) formalism to describe the tidal field of anisotropic halo-centric density distributions, as characterised by the halo-centric tidal tensor $\langle T_{ij} \rangle (< R)$ spherically averaged on scale $R \sim 4R_{\text{vir}}$ for haloes of virial radius R_{vir} . We focus on axisymmetric anisotropies, which allows us to explore simple and intuitive toy models of (sub)halo configurations that exemplify some of the most interesting anisotropies in the cosmic web. We build our models around the spherical Navarro-Frenk-White (NFW) profile after describing it as a Gaussian mixture, which leads to almost fully analytical expressions for the ‘tidal anisotropy’ scalar $\alpha(< 4R_{\text{vir}})$ extracted from the tidal tensor. Our axisymmetric examples include (i) a spherical halo at the axis of a cylindrical filament, (ii) an off-centred satellite in a spherical host halo and (iii) an axisymmetric halo. Using these, we demonstrate several interesting results. For example, the tidal tensor at the axis of a pure cylindrical filament gives $\alpha^{(\text{fil})}(< R) = 1/2$ exactly, for any R . Also, $\alpha(< 4R_{\text{vir,sat}})$ for a satellite of radius $R_{\text{vir,sat}}$ as a function of its host-centric distance is a sensitive probe of dynamical mass loss of the satellite in its host environment. Finally, we discuss a number of potentially interesting extensions and applications of our formalism that can deepen our understanding of the multi-scale phenomenology of the cosmic web.

Key words: cosmology: theory, dark matter, large-scale structure of the Universe – methods: analytical, numerical

1 INTRODUCTION

The cosmic tidal environment of dark matter haloes is a key arbiter of their growth and evolution, and possibly also of the physics governing the galaxies that occupy them. Early work in this subject (Zel’dovich 1970; Doroshkevich 1970; Shandarin & Zeldovich 1989) has established the important role of tidal fields in the formation of the cosmic web, with subsequent numerical work (Bond & Myers 1996a,b,c; Bond et al. 1996) showing that the skeleton of the cosmic web is already in place when the bulk of formation of small-scale structure occurs (see also van de Weygaert & Bond 2008). Due to the non-linearity of gravitational evolution, most of the progress in our understanding of the connection between cosmic tidal fields and the physics of haloes and galaxies has been driven by numerical simulations (Hoffman 1986; van de Weygaert & Babul 1993; van Haarlem & van de Weygaert 1993; Hahn et al. 2007a,b, 2009; Codis et al. 2012; Behroozi et al. 2014; Chisari et al. 2015; Hearin et al. 2016; Borzyszkowski et al. 2017; Paranjape et al. 2018; Libeskind et al. 2018; Kraljic et al. 2019). Analytical insight, however,

can play an important role in clarifying the multitude of multi-scale correlations (see, e.g., Han et al. 2019; Ramakrishnan et al. 2019) that pervade the cosmic web.

The cosmic web is generally decomposed into its component structures that include filaments and sheets (or walls), with nodes occurring at the intersections of filaments and voids filling most of the intervening volume. These structures are usually quantified either using the spatial variation of the density field or using the strength of the tidal field (see, e.g., Libeskind et al. 2018, and references therein). In this work, we will focus on using the cosmic tidal field as a means of classifying the cosmic web (Hahn et al. 2007a; Forero-Romero et al. 2009; see also Cautun et al. 2013).

There have been several (semi-)analytical studies of tidal fields starting from the seminal work of Zel’dovich (1970), particularly on the role of initial tides in determining late-time halo distributions (see, e.g., Icke 1973; White & Silk 1979; Eisenstein & Loeb 1995; Bond & Myers 1996a; van de Weygaert & Bertschinger 1996; Monaco 1999; Sheth et al. 2001a; Shen et al. 2006; Desjacques 2008; Rossi 2012; Pápai & Sheth 2013; Castorina et al. 2016; Musso et al. 2018; Desjacques et al. 2018). The evolution of the cosmic web is also predicted to be intimately tied with the acquisition of

* E-mail: aseem@iucaa.in

angular momentum by haloes and consequently the galaxies that inhabit them. Although not the focus of this work, it is worth mentioning that tidal torque theory (Hoyle 1951; Peebles 1969; White 1984) explicitly models the effect of the tidal environment on evolving proto-halo patches, thus imbuing them with angular momentum, both in the linear and non-linear regime (e.g., Lee & Pen 2000; Porciani et al. 2002b,a; Aragón-Calvo et al. 2007; Hahn et al. 2007a; Jones & van de Weygaert 2009; Schäfer 2009). In parallel, there is also a well-developed analytical framework for studying spherical haloes and their spatial distribution (the halo model, see Cooray & Sheth 2002, for a review). However, the non-linear analytical modelling of small-scale, late-time cosmic web environments remains largely unexplored.

To this end, in this work we develop the analytical framework needed to describe the key variable of interest, namely, the halo-centric tidal tensor T (defined below) spherically averaged with a smoothing scale R proportional to the halo virial radius R_{vir} . The expressions for the smoothed tensor $T(< R)$ can then be reduced to the scalar halo-centric ‘tidal anisotropy’ $\alpha(< 4R_{\text{vir}})$ (see below) which has emerged as a particularly useful indicator of the local cosmic web environment of the halo. This quantity correlates tightly with the large-scale environment (or linear halo bias b_1) of dark matter haloes over a wide range of halo mass (Paranjape et al. 2018). It also correlates tightly with a number of internal halo properties such as halo concentration, the anisotropy of the mass and velocity ellipsoid tensors, the anisotropy of velocity dispersion and halo spin (Ramakrishnan et al. 2019). In fact, Ramakrishnan et al. (2019) showed that the assembly (or secondary) bias, i.e., the correlation $c \leftrightarrow b_1$ at fixed halo mass (Sheth & Tormen 2004; Gao et al. 2005; Jing et al. 2007; Faltenbacher & White 2010) seen in *all* of these internal properties c can be statistically explained as arising from the two fundamental correlations $\alpha \leftrightarrow b_1$ and $\alpha \leftrightarrow c$. It is therefore of considerable interest to gain analytical insights into the behaviour of $\alpha(< 4R_{\text{vir}})$ in different cosmic web environments.

We will see that the tidal tensor formalism we develop considerably simplifies for an axisymmetric unsmoothed density field. We will therefore apply this restricted, axisymmetric version of our analytical framework to three toy models: (i) a halo at the axis of a filament, (ii) a satellite in a spherical halo and (iii) an axisymmetric halo, all built around the spherical NFW profile (Navarro, Frenk & White 1996, 1997). These examples are chosen to minimally illustrate a few of the most relevant anisotropies that are expected to affect (sub)halo populations in the cosmic web, and represent a trade-off between analytical simplicity and cosmological relevance. Throughout, we adopt a ‘halo modeller’ point of view, in that we aim to describe static cosmological configurations rather than predict their dynamical evolution. Nevertheless, we will see that our models can, in principle, be used to place interesting constraints on dynamical models as well.

Despite the restriction to axisymmetric anisotropies, the integrals defining the tidal tensor do not have closed form expressions, in general. We therefore introduce a high-accuracy Gaussian mixtures description of the NFW profile. While increasing the complexity of the profile itself, this allows for expressions for the tidal tensor that are either in closed form or involve straightforward 1-dimensional numerical integrals, in all the cases we study. We perform the Gaussian mixture

fit using an implementation of a non-negative least squares algorithm in standard numerical libraries. Calculating the full tidal tensor is then essentially reduced to a trivial numerical book-keeping exercise in combining the contributions from individual Gaussian components.

The paper is organised as follows. Section 2 sets up the tidal tensor formalism in spherical polar coordinates, focusing on spherically averaged quantities described using spherical harmonics. Section 3 presents the Gaussian mixture description of the NFW profile. Section 4 applies the resulting framework to the examples mentioned above and we conclude in section 5. The Appendices present details of calculations used in the main text. Unless stated otherwise, for illustrative purposes we will use $c_{\text{vir}} = 7 (R_{\text{vir}}/1h^{-1}\text{Mpc})^{-0.4}$ for the halo concentration of the NFW profile, which is approximately consistent with the relation calibrated by Bullock et al. (2001) using haloes in N -body simulations.¹

2 ANALYTICAL FORMALISM: TIDAL TENSOR

In this section we derive our main formal results, namely, expressions for the spherically averaged halo-centric tidal tensor (defined below). Although the formalism can be developed in full generality, for analytical simplicity we eventually focus attention on the tidal tensor derived from an axisymmetric field.

2.1 Basic definitions

The primary quantity of our interest is the dimensionless tidal tensor $T(\mathbf{r})$ at location \mathbf{r} which can be written in coordinate invariant form as

$$T(\mathbf{r}) = (\nabla \otimes \nabla) \psi(\mathbf{r}), \quad (1)$$

where \otimes denotes a direct product, ∇ is the gradient operator and $\psi(\mathbf{r})$ is the normalised gravitational potential which obeys the Poisson equation

$$\nabla^2 \psi(\mathbf{r}) = \delta(\mathbf{r}), \quad (2)$$

where

$$\delta(\mathbf{r}) \equiv \Delta(\mathbf{r}) - 1 = \rho(\mathbf{r})/\bar{\rho} - 1 \quad (3)$$

is the matter density contrast (and is also consequently the trace of the tidal tensor). Typically, one considers spherically averaged versions of Δ and ψ . For any field $f(\mathbf{r})$ with Fourier transform coefficients $f_{\mathbf{k}}$, the smoothed field can be written as

$$f(\mathbf{r}; < R) = \mathcal{F}[f_{\mathbf{k}} W(\mathbf{k}; R)] \quad (4)$$

where $W(\mathbf{k}; R) = W(kR)$ is the Fourier transform of the normalised spherical smoothing window and R is the smoothing radius. E.g., the Gaussian window routinely employed in simulations would have $W(kR) = e^{-k^2 R^2/2}$. Below, we will exclusively consider spherical tophat averaging, for which

¹ It is straightforward to incorporate more up-to-date calibrations such as those presented by Diemer & Kravtsov (2015); however, this will not alter any of our conclusions.

$W(kR) = 3j_1(kR)/(kR)$ with $j_1(x)$ a spherical Bessel function. We will drop the explicit dependence on location and/or smoothing scale in $f(\mathbf{r}; < R)$ whenever no confusion can arise.

The (smoothed) tidal tensor can be diagonalised at each location; we denote its three eigenvalues as

$$\lambda_1 \leq \lambda_2 \leq \lambda_3, \quad (5)$$

and we have $\Delta - 1 = \lambda_1 + \lambda_2 + \lambda_3$. The eigenvalues can be combined into the ‘tidal anisotropy’ α defined as

$$\alpha \equiv \sqrt{q^2}/\Delta, \quad (6)$$

with

$$q^2 \equiv \frac{1}{2} [(\lambda_3 - \lambda_1)^2 + (\lambda_3 - \lambda_2)^2 + (\lambda_2 - \lambda_1)^2]. \quad (7)$$

For the reasons discussed in the Introduction, it is of considerable interest to understand the properties of $\alpha(\mathbf{r}_{\text{halo}}; < 4R_{\text{vir}})$ for a halo of virial radius R_{vir} located at \mathbf{r}_{halo} in a variety of cosmic web environments and halo configurations. We will do so below using toy models which, despite being considerably simplified, yield valuable insight into the nature of the anisotropic cosmic tidal field.

2.2 Tidal tensor in polar coordinates

We are interested in describing spherically averaged tidal fields derived from anisotropic density distributions centred on halo locations. It is therefore convenient to perform all calculations using spherical polar coordinates $\{r, \theta, \phi\}$ along with spherical harmonic multipole expansions. We set up this formalism for the tidal tensor next. To start with, let us obtain the spherical polar components of T (equation 1) in spherical coordinates. We will then use these to describe the spherically averaged *Cartesian* components of T , which will lead in a straightforward manner to expressions for $\alpha(< R)$.

Denoting the spherical polar orthonormal basis vectors as $\{\mathbf{e}_\alpha\} = \{\mathbf{e}_r, \mathbf{e}_\theta, \mathbf{e}_\phi\} = \{\hat{r}, \hat{\theta}, \hat{\phi}\}$ and partial derivatives as $\partial/\partial r = \partial_r$, etc., and writing the tidal tensor as $T = T_{\alpha\beta}(\mathbf{e}_\alpha \otimes \mathbf{e}_\beta)$, the spherical polar components $T_{\alpha\beta}$ can then be expressed in terms of spherical polar derivatives of ψ using the expression

$$\nabla = \hat{r} \partial_r + \frac{1}{r} \hat{\theta} \partial_\theta + \frac{1}{r \sin \theta} \hat{\phi} \partial_\phi \equiv \hat{r} \partial_r + \frac{1}{r} \nabla_\Omega, \quad (8)$$

along with derivative identities relating the basis vectors. Here and below, we abbreviate $\sin(\theta) = s_\theta$ and $\cos(\theta) = c_\theta$ for any angle θ . Appendix A1 shows that this results in the expressions

$$\begin{aligned} T_{rr} &= \partial_r^2 \psi \quad ; \quad T_{\theta\theta} = \frac{1}{r} \partial_r \psi + \frac{1}{r^2} \partial_\theta^2 \psi \\ T_{\phi\phi} &= \frac{1}{r} \partial_r \psi + \frac{1}{r^2} \frac{c_\theta}{s_\theta} \partial_\theta \psi + \frac{1}{(r s_\theta)^2} \partial_\phi^2 \psi \\ T_{r\theta} &= \frac{1}{r^2} (r \partial_r - 1) \partial_\theta \psi \quad ; \quad T_{r\phi} = \frac{1}{r^2 s_\theta} (r \partial_r - 1) \partial_\phi \psi \\ T_{\theta\phi} &= \frac{1}{r^2 s_\theta} \left(\partial_\theta - \frac{c_\theta}{s_\theta} \right) \partial_\phi \psi. \end{aligned} \quad (9)$$

Appendix A1 also relates these spherical polar components $T_{\alpha\beta}(\mathbf{r})$ to the more familiar Cartesian components $T_{ij}(\mathbf{r})$, $i, j \in \{x, y, z\}$ using a local rotation of basis vectors at \mathbf{r} . These are summarised in equation (A7).

2.3 Spherical averaging

We are interested in spherically averaging the halo-centric tidal tensor equation (9). In general, for any quantity $T(\mathbf{r})$ expressed in spherical polar coordinates, smoothing with a spherical tophat of radius R can be written as an angular average followed by a radial average, i.e.,

$$\langle T \rangle(< R) \equiv \langle \langle T \rangle_\Omega \rangle_R \quad (10)$$

where the angular average is defined by

$$\begin{aligned} \langle f \rangle_\Omega &\equiv \int \frac{d\Omega}{4\pi} f(\mu, \phi) \\ &= \int_{-1}^1 \frac{d\mu}{2} \int_0^{2\pi} \frac{d\phi}{2\pi} f(\mu, \phi) \\ &\equiv \langle \langle f \rangle_\phi \rangle_\mu, \end{aligned} \quad (11)$$

where we defined

$$\mu \equiv \cos(\theta), \quad (12)$$

and the average over radial shells is

$$\langle g \rangle_R \equiv \frac{3}{R^3} \int_0^R dr r^2 g(r). \quad (13)$$

In the following, we will also use the notation $g(< R)$ to denote the average (13) of any radial function $g(r)$.

2.4 Multipole expansions

Writing $\mathbf{r} = r \hat{r}(\mu, \phi)$, we can expand the *unsmoothed*, halo-centric gravitational potential $\psi(\mathbf{r})$ and local overdensity $\Delta(\mathbf{r})$ in spherical harmonics as

$$\psi(\mathbf{r}) = \sum_{\ell=0}^{\infty} \sum_{m=-\ell}^{\ell} \psi_{\ell m}(r) Y_\ell^m(\hat{r}) \quad (14)$$

$$\Delta(\mathbf{r}) - 1 = \sum_{\ell=0}^{\infty} \sum_{m=-\ell}^{\ell} \Delta_{\ell m}(r) Y_\ell^m(\hat{r}), \quad (15)$$

(note the -1 on the l.h.s. of equation 15) where $Y_\ell^m(\hat{r})$ are spherical harmonics. Appendix A2 recapitulates some useful properties of the $Y_\ell^m(\hat{r})$ and Legendre polynomials $P_\ell(\mu)$.

Using the multipole expansion of the Green’s function of the Laplacian ∇^2 , the Poisson equation can be integrated in spherical polar coordinates to obtain the solution (Binney & Tremaine 1987, section 2.4)

$$\psi_{\ell m}(r) = -\frac{1}{2\ell+1} \left[\frac{1}{r^{\ell+1}} \mathcal{I}_{\ell m}(r) + r^\ell \mathcal{O}_{\ell m}(r) \right], \quad (16)$$

where we defined

$$\begin{aligned} \mathcal{I}_{\ell m}(r) &= \int_0^r du u^2 u^\ell \Delta_{\ell m}(u) \\ \mathcal{O}_{\ell m}(r) &= \int_r^\infty du u^2 \frac{1}{u^{\ell+1}} \Delta_{\ell m}(u). \end{aligned} \quad (17)$$

Armed with a model for the anisotropy of the density distribution given by the functions $\Delta_{\ell m}(r)$, we can then use equations (14) and (16) to evaluate the tidal tensor components in equation (9) at any location.

2.5 Axisymmetric model

In principle, one could now sequentially perform the azimuthal, polar and radial averages of the tidal tensor and then calculate α using equations (6), (7) and (A9). Appendix A3 presents the azimuthal average of the tidal tensor; this shows that *all* Cartesian components of the tidal tensor are, in general, non-vanishing, which makes the subsequent steps rather involved. To simplify the discussion, in the following we will therefore *restrict attention to axisymmetric potentials described by $m = 0$ but generic ℓ , for which the angle-averaged tidal tensor is diagonal in the Cartesian frame* (equation A21 in Appendix A4), and will return to a fuller discussion of generic potentials in future work.

Since the tidal tensor T is linear in the potential ψ , which is itself linear in overdensity Δ , we can analyse each multipole moment separately to begin with. For a pure multipole ℓ , restricting to $m = 0$, we have

$$\psi(\mathbf{r}) = N_{\ell 0} P_{\ell}(\mu) \psi_{\ell 0}(r), \quad (18)$$

where the normalisation constant $N_{\ell m}$ is defined in equation (A15) and included here for convenience.

Appendix A4 also shows that the angle-averaging the Cartesian components of the tidal tensor derived from equation (18) kills all multipoles except $\ell = 0$ and $\ell = 2$, leading to

$$\begin{aligned} \langle T_{xx} \rangle_{\Omega} &= \frac{1}{3} [\langle \Delta \rangle_{\Omega}(r) - 1] \delta_{\ell,0} + \frac{1}{2} t(r) \delta_{\ell,2} = \langle T_{yy} \rangle_{\Omega} \\ \langle T_{zz} \rangle_{\Omega} &= \frac{1}{3} [\langle \Delta \rangle_{\Omega}(r) - 1] \delta_{\ell,0} - t(r) \delta_{\ell,2}. \end{aligned} \quad (19)$$

where

$$\langle \Delta \rangle_{\Omega}(r) - 1 = N_{00} \Delta_{00} = N_{00} r^{-2} \partial_r(r^2 \partial_r \psi_{00}), \quad (20)$$

and we defined

$$t(r) \equiv -\frac{1}{3} \sqrt{\frac{1}{5\pi}} \left[\psi''_{20} + \frac{5}{r} \psi'_{20} + \frac{3}{r^2} \psi_{20} \right]. \quad (21)$$

Performing the radial average and generalising to an arbitrary axisymmetric density field satisfying

$$\Delta(\mathbf{r}) - 1 = \sum_{\ell=0}^{\infty} N_{\ell 0} P_{\ell}(\mu) \Delta_{\ell 0}(r), \quad (22)$$

$$\Delta_{\ell 0}(r) = 4\pi N_{\ell 0} \int_{-1}^1 \frac{d\mu}{2} P_{\ell}(\mu) (\Delta(\mathbf{r}) - 1), \quad (23)$$

the Cartesian components of the spherically averaged tidal tensor can be written as

$$\langle T_{ij} \rangle(< R) = \text{diag} \{ \lambda_+, \lambda_+, \lambda_- \} \quad (24)$$

with

$$\begin{aligned} \lambda_+ &\equiv \frac{1}{3} [\langle \Delta \rangle(< R) - 1] + \frac{1}{2} t(< R), \\ \lambda_- &\equiv \frac{1}{3} [\langle \Delta \rangle(< R) - 1] - t(< R), \end{aligned} \quad (25)$$

where $t(< R)$ is the radial average of $t(r)$ (equation 13) and can be written using straightforward integration by parts as

$$\begin{aligned} t(< R) &= -\frac{1}{\sqrt{5\pi}} \left(\frac{1}{r^4} \partial_r (r^3 \psi_{20}(r)) \right) \Big|_{r=R} \\ &= \frac{1}{\sqrt{5\pi}} \int_R^{\infty} \frac{dr}{r} \Delta_{20}(r), \end{aligned} \quad (26)$$

with the second equality following from equations (16) and (17), and we have

$$\begin{aligned} \langle \Delta \rangle(< R) - 1 &= \frac{1}{\sqrt{4\pi}} \Delta_{00}(< R) \\ &= \frac{3}{\sqrt{4\pi}} \left(\frac{1}{r} \partial_r \psi_{00}(r) \right) \Big|_{r=R}. \end{aligned} \quad (27)$$

Using equation (7), we then have

$$q^2(< R) = (\lambda_+ - \lambda_-)^2 = \left(\frac{3}{2} t(< R) \right)^2, \quad (28)$$

and the tidal anisotropy $\alpha(< R)$ in equation (6) for a generic axisymmetric density field is thus given by

$$\alpha(< R) = \frac{3}{2} \frac{|t(< R)|}{\langle \Delta \rangle(< R)}. \quad (29)$$

Equations (26), (27) and (29), valid for any axisymmetric density distribution (22), form the core result of this work.

2.6 Special cases

Before exploring applications of these results, we pause to consider two interesting off-shoots of our calculations above.

2.6.1 Density Hessian

It is interesting to compare the calculation of the tidal tensor above with the closely related density Hessian

$$H \equiv (\nabla \otimes \nabla)(\Delta - 1). \quad (30)$$

The spherically averaged density Hessian is also diagonal in the Cartesian frame in the axisymmetric model. We can directly apply the formalism above to write

$$\langle H_{ij} \rangle(< R) = \text{diag} \{ \Lambda_+, \Lambda_+, \Lambda_- \}, \quad (31)$$

with

$$\begin{aligned} \Lambda_+ &\equiv \frac{1}{3} \chi(< R) + \frac{1}{2} \tau(< R), \\ \Lambda_- &\equiv \frac{1}{3} \chi(< R) - \tau(< R), \end{aligned} \quad (32)$$

where

$$\chi(< R) = \frac{3}{\sqrt{4\pi}} \left(\frac{1}{r} \partial_r \Delta_{00}(r) \right) \Big|_{r=R}, \quad (33)$$

$$\tau(< R) = -\frac{1}{\sqrt{5\pi}} \left(\frac{1}{r^4} \partial_r (r^3 \Delta_{20}(r)) \right) \Big|_{r=R}. \quad (34)$$

In other words, the spherically averaged tidal tensor and density Hessian are perfectly aligned in the axisymmetric model. Since this was a direct consequence of assuming that only $m = 0$ contributes (see, e.g., equation A19), *any misalignment of the tidal tensor and density Hessian must be directly connected to departures from axisymmetry of the density distribution*. In other words, the misalignment angle between these two *smoothed* tensors can be thought of as a direct measurement of triaxiality of the *unsmoothed* field.

2.6.2 Perfect spherical symmetry

It is also instructive to recover the tidal tensor for a perfectly spherically symmetric density field from the formalism above. When $\Delta(\mathbf{r}) = \Delta(r)$, only the monopole $\ell = 0$, $m = 0$ survives in equation (16) so that $\psi(\mathbf{r}) = \psi(r)$ satisfies $r^{-2}\partial_r(r^2\partial_r\psi(r)) = \Delta(r) - 1$, and equation (1) consequently becomes the diagonal form

$$\begin{aligned} T &= (\hat{r} \otimes \hat{r}) \partial_r^2 \psi + \left(\hat{\theta} \otimes \hat{\theta} + \hat{\phi} \otimes \hat{\phi} \right) \frac{1}{r} \partial_r \psi \\ &= \frac{1}{3} \mathbf{1} \left(\frac{3}{r} \partial_r \psi \right) + (\hat{r} \otimes \hat{r}) \left(\partial_r^2 \psi - \frac{1}{r} \partial_r \psi \right) \\ &= \frac{1}{3} \mathbf{1} (\Delta(r) - 1) + \left(\frac{1}{3} \mathbf{1} - \hat{r} \otimes \hat{r} \right) (\Delta(< r) - \Delta(r)), \end{aligned} \quad (35)$$

where $\mathbf{1} = \hat{r} \otimes \hat{r} + \hat{\theta} \otimes \hat{\theta} + \hat{\phi} \otimes \hat{\phi}$ is the identity matrix. This agrees with Pápai & Sheth (2013), with the first term being the isotropic part proportional to the differential density contrast $\Delta(r) - 1$ and the second term being the trace-free contribution.

It is also interesting to note that the angle average of this tensor $\langle T \rangle_\Omega$ completely kills the trace-free part. This is easily seen by converting equation (35) to Cartesian components using equation (A7) and then using the identities (A20) and $\langle \mu^2 \rangle_\mu = 1/3$, which leads to $\langle T \rangle_\Omega = \mathbf{1} (\Delta(r) - 1)/3$, which agrees with equation (19) for the case where only the monopole $\ell = 0$ contributes. Radially averaging this gives $\langle T \rangle(< R) = \mathbf{1} (\Delta(< R) - 1)/3$; thus, the spherical average of a spherically symmetric tidal tensor is isotropic. *Any anisotropy in the spherically averaged halo-centric tidal tensor is therefore a direct consequence of anisotropy in the unsmoothed density field.*

3 ANALYTICAL FORMALISM: SPHERICAL PROFILES

In this section, we develop a Gaussian mixtures approach to describing spherically symmetric density profiles, which considerably simplifies the application of the tidal tensor formalism to interesting halo model configurations. We remind the reader that we are interested in developing a descriptive framework rather than tracking dynamical evolution, and therefore assume pre-existing, non-linearly evolved density profiles for the halo interior, wherever needed.

3.1 The NFW profile

As our base spherical profile, we will use the 2-parameter isotropic NFW profile (Navarro et al. 1996, 1997), which provides a simple and accurate description of the spherically averaged dark matter density profile of haloes identified in N -body simulations. The profile is given by

$$\Delta_{\text{NFW}}(r|R_{\text{vir}}, c_{\text{vir}}) = \frac{\Delta_{\text{vir}}}{3} \frac{c_{\text{vir}}^3}{f(c_{\text{vir}})} \frac{1}{(r/r_s)(1 + r/r_s)^2}, \quad (36)$$

where R_{vir} and c_{vir} are, respectively, the virial radius and concentration of the halo, in terms of which the scale radius r_s satisfies

$$r_s = R_{\text{vir}}/c_{\text{vir}}, \quad (37)$$

and we defined the function

$$f(c) \equiv \int_0^c \frac{dy y}{(1+y)^2} = \ln(1+c) - \frac{c}{1+c}. \quad (38)$$

The profile (36) is normalised so as to enclose a mass $m_{\text{vir}} = (4\pi/3)R_{\text{vir}}^3\Delta_{\text{vir}}\bar{\rho}$ inside the virial radius, i.e.,

$$\Delta_{\text{NFW}}(< R_{\text{vir}}|R_{\text{vir}}, c_{\text{vir}}) = \Delta_{\text{vir}}. \quad (39)$$

3.2 Gaussian mixtures description

We wish to explore anisotropic (axisymmetric) models built around the spherical NFW profile (36). Despite its simplicity and the fact that analytical results exist in closed form for many associated properties such as the gravitational potential, velocity dispersion, etc. (see, e.g., Sheth et al. 2001b), the integrals involved in computing the spherical harmonic coefficients $\Delta_{\ell 0}(r)$ for the axisymmetric model (equation 23) do not typically have closed form expressions. However, a spherically symmetric *Gaussian* profile $\propto e^{-r^2/R_*^2}$ for some scale radius R_* , does in fact lead to almost fully analytical expressions for $\langle \Delta \rangle(< R)$ and $t(< R)$ for the models we explore.

In the following, therefore, we approximate the original isotropic NFW function with a Gaussian mixture,

$$\Delta_{\text{NFW}}(r|R_{\text{vir}}, c_{\text{vir}}) = \sum_j w_j \Delta_G(r|\sigma_j, r_s), \quad (40)$$

with r_s given by equation (37) and where

$$\Delta_G(r|\sigma_j, r_s) = \Delta_j e^{-r^2/(2r_s^2\sigma_j^2)}, \quad (41)$$

with pre-decided (dimensionless) widths $\{\sigma_j\}$ and normalisations $\{\Delta_j\}$. Our choice of widths σ_j and the number of components is described in Appendix B. The weights $\{w_j\}$ are determined by a non-negative least squares calculation (Lawson & Hanson 1995) subject to the constraint

$$\sum_j w_j = 1. \quad (42)$$

Appendix B summarises our implementation. We normalise each Gaussian component (41) so as to enclose the *same* mass m_{vir} inside R_{vir} as the full NFW profile, i.e., we demand $\Delta_G(< R_{\text{vir}}|\sigma_j, r_s) = \Delta_{\text{vir}}$ for each j , obtaining

$$\Delta_j = \frac{\Delta_{\text{vir}}}{3} \frac{c_{\text{vir}}^3}{g(c_{\text{vir}}|\sigma_j)}, \quad (43)$$

where we defined the function

$$\begin{aligned} g(c|\sigma) &\equiv \int_0^c dy y^2 e^{-y^2/(2\sigma^2)} \\ &= \sqrt{\frac{\pi}{2}} \sigma \operatorname{erf}\left(\frac{c}{\sqrt{2}\sigma}\right) - \sigma^2 c e^{-c^2/(2\sigma^2)}. \end{aligned} \quad (44)$$

With this choice of normalisation, the weights $\{w_j\}$ correspond to the mass fraction contributed by the respective Gaussian components.

Figure 1 shows the results of the Gaussian mixture fit for two combinations of R_{vir} and c_{vir} . The Gaussian mixture is naturally adapted to describing the profiles measured in actual N -body simulations which have finite force resolution r_{force} which leads to a flattening (or core) in the measured profile at $r \lesssim r_{\text{force}}$. This can be trivially mimicked by the

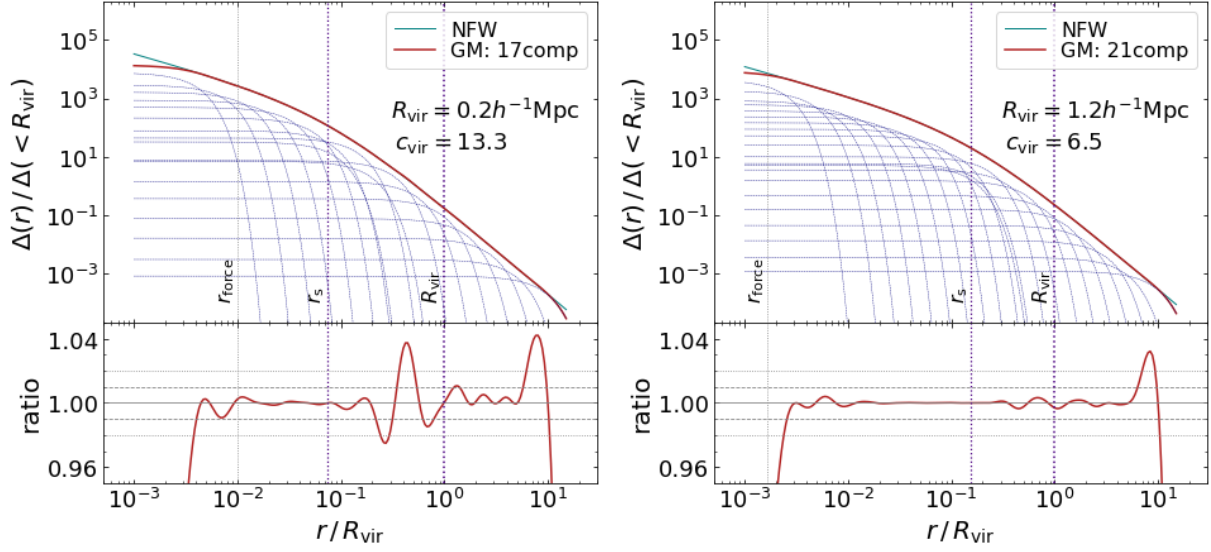


Figure 1. Gaussian mixture approximations for the NFW profile for two combinations of virial radius R_{vir} and concentration c_{vir} , corresponding to a small ($m_{\text{vir}} \simeq 2 \times 10^{12} h^{-1} M_{\odot}$; *left panels*) and a large halo ($m_{\text{vir}} \simeq 4 \times 10^{14} h^{-1} M_{\odot}$; *right panels*). (*Top row:*) Cyan curves in each panel show the original NFW profile (36), normalised to enclose unit density inside R_{vir} and shown as a function of halo-centric distance r in units of R_{vir} . Red curves show the corresponding best fitting Gaussian mixture (40) with the number of components indicated in the respective legend. Thin purple curves show individual Gaussian components. (*Bottom row:*) Ratio of the Gaussian mixture to the original NFW profile. The fits were performed using a constrained non-linear least squares method as described in section 3.2 and Appendix B, setting the “force resolution” $r_{\text{force}} = 2 h^{-1} \text{kpc}$. Vertical dotted lines in each panel indicate the values (from left to right) of r_{force} , scale radius $r_s = R_{\text{vir}}/c_{\text{vir}}$ and R_{vir} . For these examples, we see sub-percent deviations between the fit and the original profile over nearly the entire dynamic range explored, except for local peaks and troughs reaching inaccuracies of a few per cent. See Figure 2 for a comprehensive summary of errors in the fits over the parameter space of $\{R_{\text{vir}}, c_{\text{vir}}\}$.

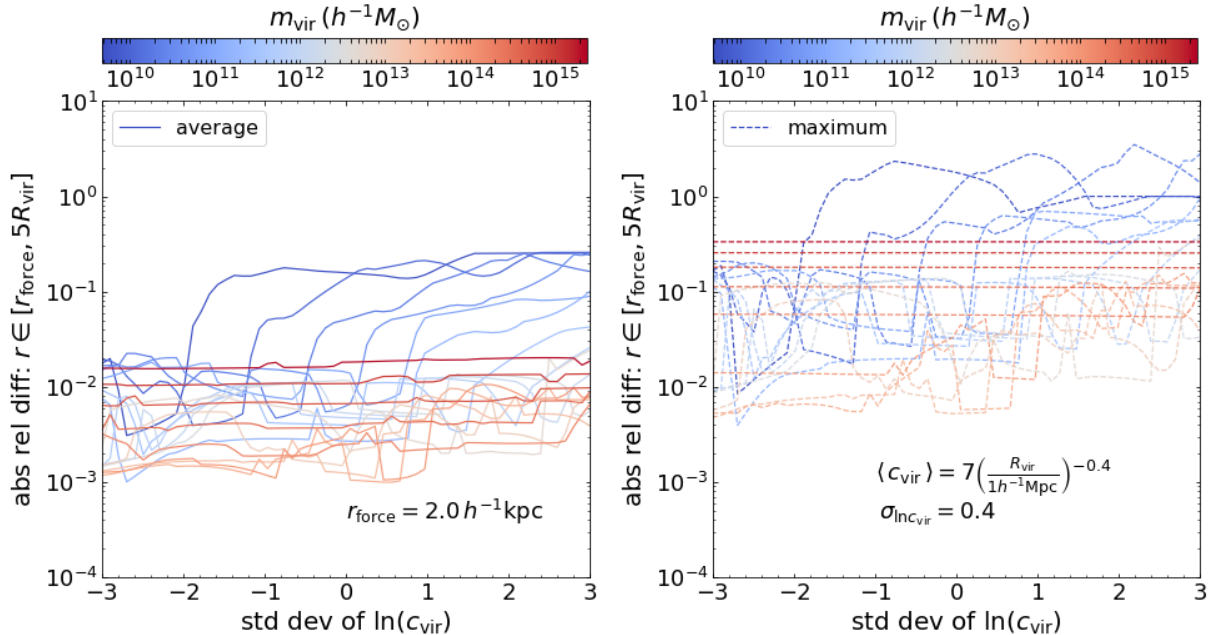


Figure 2. Average (*left panel*) and maximum (*right panel*) of the absolute relative difference $\epsilon \equiv |\Delta_{\text{GM}}(r)/\Delta_{\text{NFW}}(r) - 1|$ between the NFW profile (36) and its Gaussian mixture approximation (40) measured in the range $r \in [r_{\text{force}}, 5R_{\text{vir}}]$ for a range of values of halo virial mass m_{vir} (indicated by the colour bar) and as a function of the standardised scatter of halo concentration c_{vir} away from the median value at fixed halo mass, assuming a lognormal distribution with width $\sigma_{\ln c_{\text{vir}}} = 0.4$ (Wechsler et al. 2002). For the median concentration we use $\langle c_{\text{vir}} \rangle = 7 (R_{\text{vir}}/1 h^{-1} \text{Mpc})^{-0.4}$ which is approximately consistent with the relation calibrated by Bullock et al. (2001) (using more up-to-date calibrations does not change the results). The average value of ϵ remains below $\sim 1\%$ for all but the smallest and largest haloes we consider, at nearly all concentrations. The maximum is similarly better than $\sim 20\%$ except for the smallest and largest haloes. Note that the range $[r_{\text{force}}, 5R_{\text{vir}}]$ spans nearly 3 orders of magnitude in halo-centric distance for $m_{\text{vir}} \gtrsim 10^{14} h^{-1} M_{\odot}$. See also Figure 1.

Gaussian mixture by simply dropping the appropriate number of components with the smallest σ_j values. The fits in Figure 1 were constructed to safely describe the NFW profile in simulations with $r_{\text{force}} \geq 2h^{-1}\text{kpc}$ at $z = 0$.

Figure 2 shows the average (*left panel*) and maximum (*right panel*) of the absolute relative difference between the actual NFW profile and its Gaussian mixture, measured in the range $[r_{\text{force}}, 5R_{\text{vir}}]$ with $r_{\text{force}} = 2h^{-1}\text{kpc}$, for a wide dynamic range of halo mass and concentration. We clearly obtain very high accuracy (error $\lesssim 1\%$ on average) at all but the lowest and highest masses and concentrations. Note that the range $[r_{\text{force}}, 5R_{\text{vir}}]$ spans nearly 3 orders of magnitude in halo-centric distance for $m_{\text{vir}} \gtrsim 10^{14}h^{-1}M_{\odot}$.

We also note that the reasoning in this section applies to any spherical profile (e.g., Einasto 1965; Burkert 1995; Navarro et al. 2004), particularly profiles with cores (see above), so that Gaussian mixtures can be used much more generally than for our specific choice of the NFW profile.

4 APPLICATIONS

In this section, we apply the previous formalism to build anisotropic halo models for the density and tidal environment around halo locations. We study three models, one for the tidal field experienced by a halo at the centre of a cylindrical filament, the second for an off-centred satellite in a spherical host halo and the last describing the halo-centric tidal field of an axisymmetric halo. As we saw in section 2.5, the tidal tensor formalism simplifies *considerably* for an axisymmetric unsmoothed density field. The examples we have chosen, which all involve a single special direction and are hence axisymmetric, thus represent a trade-off between analytical simplicity and cosmological relevance. Each of the examples is a toy version of more realistic configurations known or expected to exist in the cosmic web. We will also discuss potential extensions to more realistic anisotropies wherever possible.

4.1 Spherical halo in a filament

As our first example, we consider the simple case of a spherical NFW halo of radius R_{vir} and concentration c_{vir} placed *exactly on the axis* of a cylindrical filament (which we align with the Cartesian z -axis). This configuration leads to the minimum tidal anisotropy a halo can experience in a filament, since any off-axis displacements would only serve to increase the anisotropy. Figure 3 illustrates the situation.

The halo-centric dark matter overdensity at location \mathbf{r} can be written as

$$\Delta(\mathbf{r}) = \Delta^{(\text{fil})}(\mathbf{r}) + \Delta^{(\text{halo})}(\mathbf{r}), \quad (45)$$

with the superscripts on each term on the right indicating the two contributions.

The halo contribution $\Delta^{(\text{halo})}(\mathbf{r})$ is given by the spherical Gaussian mixture (40). We model the filament contribution as a single Gaussian function of the perpendicular separation $r_{\perp} = |\mathbf{r} - z\hat{z}| = r\sqrt{1 - \mu^2}$:

$$\begin{aligned} \Delta^{(\text{fil})}(\mathbf{r}) &= \frac{f_{\text{fil}}\Delta_{\text{vir}}}{2(1 - e^{-1/2})} e^{-r_{\perp}^2/(2R_f^2)} \\ &\equiv \Delta_f e^{-r^2(1 - \mu^2)/(2R_f^2)}. \end{aligned} \quad (46)$$

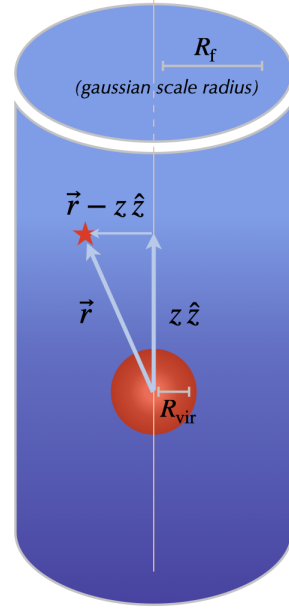


Figure 3. Illustration of a spherical NFW halo of radius R_{vir} located at the axis of a filament with a Gaussian profile (46) with scale radius R_f . The halo sees an axisymmetric tidal field due to the cylindrical density profile of the filament.

The normalisation Δ_f is chosen such that the overdensity enclosed in a cylinder of radius $r_{\perp} = R_f$ is $f_{\text{fil}}\Delta_{\text{vir}}$. Although not necessarily a realistic description of filamentary profiles, it should be clear that this model is trivially generalisable to arbitrary functional forms that can be described by a Gaussian mixture, by adding components with different choices of R_f and Δ_f .

The corresponding multipole moments (equation 23) satisfy

$$\begin{aligned} \frac{1}{\sqrt{4\pi}}\Delta_{\ell 0}^{(\text{fil})}(r) + \delta_{\ell,0} \\ = \sqrt{2\ell + 1}\Delta_f \int_{-1}^1 \frac{d\mu}{2} P_{\ell}(\mu) e^{-r^2(1 - \mu^2)/(2R_f^2)}. \end{aligned} \quad (47)$$

These can be simplified using the relation

$$\int_{-1}^1 \frac{d\mu}{2} \mu^2 e^{\mu^2 a^2} = \frac{1}{2a} \frac{d}{da} \int_{-1}^1 \frac{d\mu}{2} e^{\mu^2 a^2}, \quad (48)$$

and the identity

$$\int_{-1}^1 \frac{d\mu}{2} e^{\mu^2 a^2} = \int_0^1 d\mu e^{\mu^2 a^2} = e^{a^2} \left(\frac{\mathcal{D}(a)}{a} \right), \quad (49)$$

where $\mathcal{D}(z)$ is Dawson's integral (Abramowitz & Stegun 1972, chapter 7)

$$\mathcal{D}(z) \equiv e^{-z^2} \int_0^z dt e^{t^2}, \quad (50)$$

which can be evaluated using standard libraries (e.g., as `scipy.special.dawsn` in SciPy). For convenience below, we set

$$a \equiv \frac{r}{\sqrt{2}R_f}; \quad A \equiv \frac{R}{\sqrt{2}R_f}. \quad (51)$$

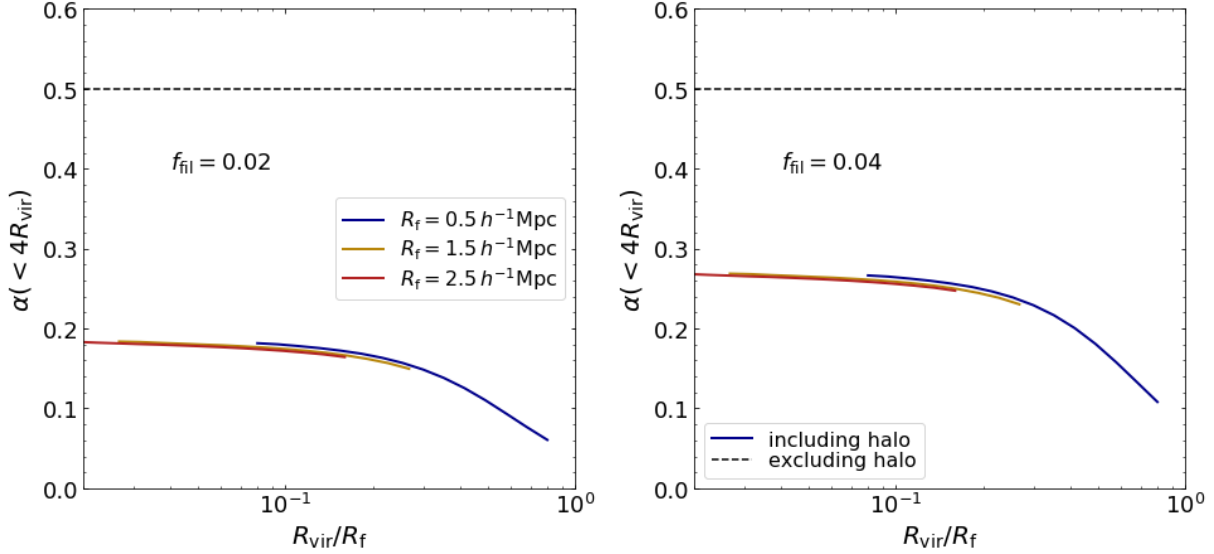


Figure 4. Tidal anisotropy $\alpha(< 4R_{\text{vir}})$ (equation 29) for a spherical NFW halo of virial radius R_{vir} placed at the axis of a cylindrical filament. The filament is chosen to have a cylindrical Gaussian density profile (46) with scale radius R_f as indicated by different colours and $f_{\text{fil}} = 0.02$ (0.04) in the *left* (*right*) panel. See Figure 3 for an illustration. Results are shown as a function of R_{vir}/R_f . Solid curves show results when including the contribution of the halo profile; these are approximately universal in R_{vir}/R_f as discussed in the text. Dashed horizontal line in each panel shows the value 1/2 obtained by ignoring the halo’s density and using only equations (54) and (55) to calculate α .

A straightforward calculation then gives

$$\frac{1}{\sqrt{4\pi}}\Delta_{00}^{(\text{fil})}(r) = \Delta_f \frac{\mathcal{D}(a)}{a}, \quad (52)$$

and

$$\frac{1}{\sqrt{5\pi}}\Delta_{20}^{(\text{fil})}(r) = \frac{3\Delta_f}{2a} \left[\frac{1}{a} - \left(\frac{2}{3} + \frac{1}{a^2} \right) \mathcal{D}(a) \right]. \quad (53)$$

Using these, the expression for $\langle \Delta^{(\text{fil})} \rangle(< R)$ becomes

$$\langle \Delta^{(\text{fil})} \rangle(< R) = \frac{3\Delta_f}{2A^2} \left(1 - \frac{\mathcal{D}(A)}{A} \right). \quad (54)$$

Remarkably, $t^{(\text{fil})}(< R)$ can also be brought to closed form in terms of Dawson’s integral; a lengthy but straightforward calculation shows that

$$\begin{aligned} t^{(\text{fil})}(< R) &= \frac{3\Delta_f}{2} \int_A^\infty \frac{da}{a^2} \left[\frac{1}{a} - \left(\frac{2}{3} + \frac{1}{a^2} \right) \mathcal{D}(a) \right] \\ &= \frac{\Delta_f}{2A^2} \left(1 - \frac{\mathcal{D}(A)}{A} \right), \end{aligned} \quad (55)$$

so that we have

$$t^{(\text{fil})}(< R) = \frac{1}{3} \langle \Delta^{(\text{fil})} \rangle(< R). \quad (56)$$

We expect this result to hold very generally. To see why, consider that a Gaussian mixture (which we expect can accurately approximate any reasonable filamentary profile) would preserve this proportionality for each component and hence also for the total. As another direct example, a straightforward calculation shows that equation (56) also holds for a power law profile $\Delta^{(\text{fil})}(\mathbf{r}) \propto (r_\perp/R_f)^{-\beta}$ with $0 < \beta < 2$, with $\langle \Delta^{(\text{fil})} \rangle(< R) \propto (R/R_f)^{-\beta}$ in this case.

Turning next to the halo self-contribution $\Delta^{(\text{halo})}(\mathbf{r})$ in equation (45), we first note that our choice of spherical symmetry for the halo means that the tidal term $t^{(\text{halo})}(< R)$

identically vanishes (section 2.6.2), while the choice of the NFW profile means that $\Delta^{(\text{halo})}(< R)$ is given by the radial average of equation (40).

Figure 4 shows the halo-centric $\alpha(< 4R_{\text{vir}})$ in this model as a function of the ratio R_{vir}/R_f , setting the filamentary relative overdensity $f_{\text{fil}} = 0.02$ (0.04) in the *left* (*right*) panel. We have used values of f_{fil} and R_f approximately consistent with the distribution shown in Figure 39 of Cautun et al. (2014); typical filaments at low redshift are expected to have overdensities $\langle \Delta \rangle \sim 10$ and thicknesses of order $\sim \text{few} \times h^{-1} \text{Mpc}$ (see also Aragón-Calvo et al. 2010; Borzyszkowski et al. 2017; Kraljic et al. 2019; Fard et al. 2019).

The solid curves show results when including the halo self-contribution as above. There are two interesting features worth discussing. First, we clearly see that large haloes in thin filaments experience a weaker anisotropy: the curves decline at large R_{vir}/R_f . On the other hand, the anisotropy approaches a constant when $R_{\text{vir}} \ll R_f$. The value of this constant depends on f_{fil} , with denser filaments (large f_{fil}) producing a larger anisotropy.

More interestingly, we see that all the curves trace out nearly universal loci of R_{vir}/R_f at fixed f_{fil} , as expected from equations (54) and (55) when the halo self-contribution is subdominant. Due to the relation (56) and the expectation that any filamentary profile can be approximated by a Gaussian mixture, we expect this near-universality to be very generally valid, with R_f being replaced by some characteristic scale describing the filament profile. The dashed line in each panel of Figure 4 shows the value 1/2 which would be obtained using equations (56) and (29) assuming the halo contribution to be completely subdominant. This serves as an upper limit to the solid curves when the smoothing radius, f_{fil} or R_f are varied.

This behaviour is particularly interesting considering

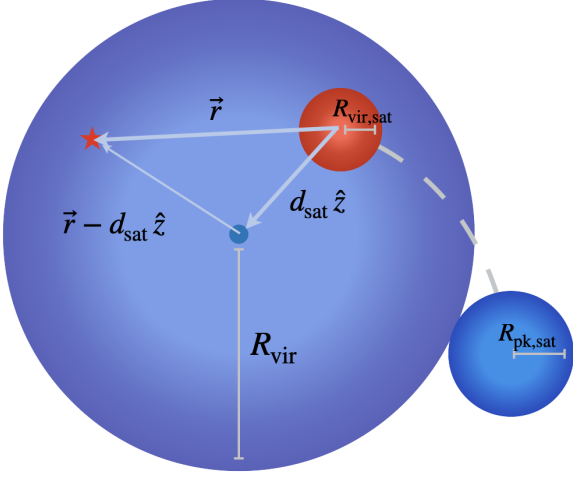


Figure 5. Illustration of a satellite of current radius $R_{\text{vir,sat}}$ located at a distance d_{sat} from the centre of its host halo which has a spherically symmetric NFW density profile with radius R_{vir} and concentration c_{vir} . The satellite is assumed to have started with a spherical NFW profile of radius $R_{\text{pk,sat}}$ and concentration $c_{\text{pk,sat}}$, which is assumed to be truncated due to mass loss as described in the text. From the vantage point of the satellite center, the spherical profile of the host is seen as having an axisymmetric anisotropy.

the fact that the value $\alpha(< 4R_{\text{vir}}) \simeq 0.5$ is known to cleanly segregate haloes living in filamentary environments from those in nodes, when filaments and nodes are defined using a counting of negative eigenvalues of the tidal tensor (see, e.g., Figure 7 of [Paranjape et al. 2018](#)). As mentioned above, we expect most realistic haloes in filaments to be found off-axis (and hence with substantially larger anisotropy than the solid curves in the Figure), with a small fraction being close to the axis. Our simple toy model then provides the first analytical explanation of why $\alpha(< 4R_{\text{vir}}) \simeq 0.5$ is a good segregator of filamentary environments: this would naturally arise if a large fraction of filamentary haloes are substantially off-axis and sub-dominant in their contribution to $\langle \Delta \rangle(< 4R)$. It will be very interesting to test these ideas by studying $\alpha(< 4R_{\text{vir}})$ as a function of the distance from the nearest filament (e.g., using filament definitions such as the one in [Sousbie 2011](#)), which we leave to future work.

4.2 Satellite in a spherical host

For our next example, consider a spherically symmetric satellite of radius $R_{\text{sat,vir}}$ located at distance d_{sat} from the centre of its spherically symmetric, NFW distributed host of radius R_{vir} and concentration c_{vir} (and hence a scale radius r_s as in equation 37). Figure 5 illustrates the situation.

The dark matter overdensity in the vicinity of the satellite has two contributions, one from the satellite's own profile and the other from the profile of the host. We write the overdensity at position \mathbf{r} as measured from the satellite's location as

$$\Delta(\mathbf{r}) = \Delta^{(\text{host})}(\mathbf{r}) + \Delta^{(\text{sat})}(\mathbf{r}), \quad (57)$$

with the superscripts on each term on the right indicating the two contributions.

4.2.1 Host contribution

Aligning the z -axis with the location of the halo centre as seen by the satellite and using the Gaussian mixture (40), it is easy to show that the host contribution is given by the axisymmetric form

$$\begin{aligned} \Delta^{(\text{host})}(\mathbf{r}) &= \Delta_{\text{NFW}}(|\mathbf{r} - d_{\text{sat}}\hat{z}| | R_{\text{vir}}, c_{\text{vir}}) \\ &= \sum_j w_j \Delta_G(|\mathbf{r} - d_{\text{sat}}\hat{z}| | \sigma_j, r_s) \\ &= \sum_j w_j \Delta_j \exp\left(-\frac{(r^2 + d_{\text{sat}}^2 - 2r d_{\text{sat}}\mu)}{2\sigma_j^2 r_s^2}\right). \end{aligned} \quad (58)$$

The corresponding multipole moments satisfy

$$\begin{aligned} \frac{1}{\sqrt{4\pi}} \Delta_{\ell 0}^{(\text{host})}(r) + \delta_{\ell,0} \\ = \sqrt{2\ell+1} \sum_j w_j \Delta_j e^{-(r^2 + d_{\text{sat}}^2)/(2\sigma_j^2 r_s^2)} \\ \times \int_{-1}^1 \frac{d\mu}{2} P_\ell(\mu) e^{\mu r d_{\text{sat}}/(\sigma_j^2 r_s^2)} \end{aligned} \quad (59)$$

Using $P_0(\mu) = 1$ and $P_2(\mu) = (3\mu^2 - 1)/2$, the integrals over μ are straightforward for $\ell = 0$ and $\ell = 2$. Defining

$$B_j \equiv d_{\text{sat}}^2/(\sigma_j^2 r_s^2), \quad (60)$$

equations (26) and (27) can be brought to the form

$$\begin{aligned} \langle \Delta^{(\text{host})} \rangle(< R) \\ = \sum_j w_j \Delta_j e^{-\frac{1}{2}B_j} \left(\frac{d_{\text{sat}}}{RB_j}\right)^3 \\ \times \int_0^{RB_j/d_{\text{sat}}} da a e^{-a^2/(2B_j)} \sinh(a), \end{aligned} \quad (61)$$

$$\begin{aligned} t^{(\text{host})}(< R) \\ = 2 \sum_j w_j \Delta_j e^{-\frac{1}{2}B_j} \left(\frac{d_{\text{sat}}}{RB_j}\right)^3 \\ \times \int_{RB_j/d_{\text{sat}}}^\infty \frac{da}{a^4} e^{-a^2/(2B_j)} \\ \times \left[(a^2 + 3) \sinh(a) - 3a \cosh(a) \right]. \end{aligned} \quad (62)$$

The integral over the auxiliary variable $a \propto r$ in equation (61) has a lengthy closed form expression in terms of error functions, which we omit for brevity. The integral in equation (62) must be performed numerically (although an asymptotic expansion, which we also omit here, is possible when $d_{\text{sat}} \ll R$).

4.2.2 Satellite contribution

Turning next to the satellite self-contribution $\Delta^{(\text{sat})}(\mathbf{r})$ in equation (57), as in section 4.1 we first note that the tidal term $t^{(\text{sat})}(< R)$ identically vanishes for our spherical satellite, and the contribution $\langle \Delta^{(\text{sat})} \rangle(< R)$ is straightforward to compute once we decide on a model for the instantaneous satellite profile.

Due to the collisionless nature of their dark matter content, satellite haloes orbiting their host rapidly lose mass due

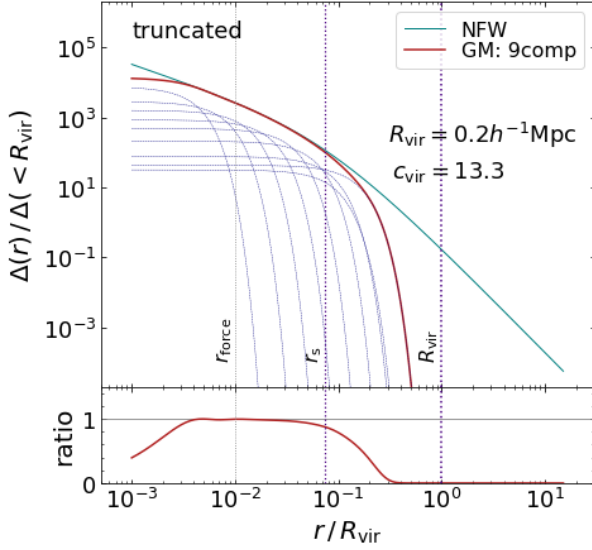


Figure 6. Example of truncated Gaussian mixture. Same as left panel of Figure 1, discarding components having $\sigma_j > c_{\text{vir}}/10$. This is useful in modelling the mass loss experienced by a satellite in a host halo. See text for a discussion.

to processes such as tidal stripping and dynamical friction. While a detailed model of the resulting profile requires substantial numerical effort (see, e.g., [van den Bosch & Ogiya 2018](#); [Ogiya et al. 2019](#); [Green & van den Bosch 2019](#)), our Gaussian mixtures approach suggests a simple and physically intuitive approximation; namely, we can *mimic satellite mass loss by simply discarding appropriately chosen Gaussian components in the outskirts* of the satellite structure (like peeling off layers of mass one at a time). Figure 6 shows an example of an NFW Gaussian mixture truncated by discarding components having $\sigma_j > c_{\text{vir}}/10$.²

More precisely, let the satellite start with an NFW profile at infall, with virial radius $R_{\text{pk,sat}}$ and concentration $c_{\text{pk,sat}} = R_{\text{pk,sat}}/r_{\text{s,sat}}$, with a corresponding Gaussian mixture $\{w_k^{(\text{sat})}, \sigma_k^{(\text{sat})}\}$ (which is obviously distinct from the host’s mixture $\{w_j, \sigma_j\}$). If the current radius of the satellite is $R_{\text{vir,sat}}$, then we model its current profile by discarding the Gaussian components having $\sigma_k^{(\text{sat})} > R_{\text{vir,sat}}/r_{\text{s,sat}}$ (recall the widths are in units of the NFW scale radius). We also assume that the satellite will be quickly disrupted if its radius becomes smaller than its initial scale radius $r_{\text{s,sat}}$, so we do not calculate α in this regime.

It remains to decide the current radius $R_{\text{vir,sat}}$, which is determined by the mass loss rate integrated over the satellite orbit. Typically, mass loss for satellites is close to being exponential in the number of dynamical times elapsed since first infall into the host (see, e.g., [van den Bosch et al. 2005](#)). Radial infall would suggest a scaling $\Delta t \propto (R_{\text{vir}} - d_{\text{sat}})^{3/2}$ for the time Δt spent by the satellite inside the host before first pericentre passage. Initial angular momentum would

modify this scaling and allow more time to be spent at larger separations from the host centre. Finally, if the satellite is outside the host ($d_{\text{sat}} > R_{\text{vir}}$), we assume there is no mass loss.³ We therefore explore the heuristic model

$$\frac{R_{\text{vir,sat}}}{R_{\text{pk,sat}}} = \min \left\{ 1, \exp \left[\frac{1}{3} \left(1 - (R_{\text{vir}}/d_{\text{sat}})^\beta \right) \right] \right\} \quad (63)$$

parametrised by β . The resulting $\langle \Delta^{(\text{sat})} \rangle(< R)$ adds to the halo contribution from equation (61) to give $\langle \Delta \rangle(< R)$, while $t(< R) = t^{(\text{host})}(< R)$ from equation (62), as we argued above.

4.2.3 Results

We are interested in the resulting behaviour of $\alpha(< 4R_{\text{vir,sat}})$. Figure 7 shows some examples using $\beta = 0.5$ and $\beta = 1.2$ (left and right columns, respectively) and large/small values of $R_{\text{pk,sat}}$ and $r_{\text{s,sat}}$ (top/bottom rows, respectively). The solid and dashed curves show results when including or excluding, respectively, the satellite self-contribution. (For the latter, we omit adding the satellite overdensity, similarly to omitting the halo contribution in section 4.1).

Several interesting features are apparent in the plots. First, the satellite self-contribution plays a dominant role in decreasing the tidal anisotropy in two regimes, both far outside the host (in all cases) and deep in its inner region (in the $\beta = 1.2$ model, just before the mass loss makes $R_{\text{vir,sat}} < r_{\text{s,sat}}$). The behaviour outside the host is easy to understand: in this regime, the satellite has a fixed NFW profile with $R_{\text{vir,sat}} = R_{\text{pk,sat}}$ in our model, while the contribution of the host to both $t(< 4R_{\text{pk,sat}})$ and $\langle \Delta \rangle(< 4R_{\text{pk,sat}})$ becomes increasingly small at larger d_{sat} . As a result, the satellite sees an increasingly isotropic environment at larger separations from the host, since we have not included any effect of the cosmic web in this model. The effect in the inner region, on the other hand, is driven by the rapid decrease of $R_{\text{vir,sat}}$ at small d_{sat} (equation 63) which leads to a rapid increase of $\langle \Delta^{(\text{sat})} \rangle(< 4R_{\text{vir,sat}})$.⁴ The corresponding increase in the host contribution $\langle \Delta^{(\text{host})} \rangle(< 4R_{\text{vir,sat}})$ is a weaker function of d_{sat} since the local density due to the host is a relatively smooth function in the satellite vicinity. This effect occurs at larger d_{sat} in the $\beta = 1.2$ model in which the decrease of $R_{\text{vir,sat}}$ is faster. In both of these regimes, we can also see that there is essentially no dependence on the virial radius and scale radius of the host.

Secondly, at separations $d_{\text{sat}} \lesssim R_{\text{vir}}$ we see a drop in the anisotropy strength whose magnitude is evidently a strong function of the relative size of the satellite to the host, but is *essentially independent of the satellite’s self-contribution*. The latter observation suggests that this effect is entirely driven by the fact that the host NFW profile is being smoothed with

³ We are also ignoring mass accretion for both satellite and host from sources other than their interaction, which would require a more detailed model of the external environment of the host.

⁴ The jaggedness apparent in the solid curves in the right panels of Figure 7 just before the curves truncate at the left, is due to the successive discrete removal of Gaussian components from the satellite profile to mimic mass loss. The jaggedness in the dashed curves at large d_{sat} , on the other hand, is due to numerical artefacts in the integral in equation (62), which converges slowly for Gaussian components with large widths.

² Alternatively, one could also build a separate, more detailed Gaussian mixture to accurately describe the shape of the truncated profile, rather than assuming the shape of the single Gaussian having the largest width of those remaining from the original mixture. We leave this to future work.

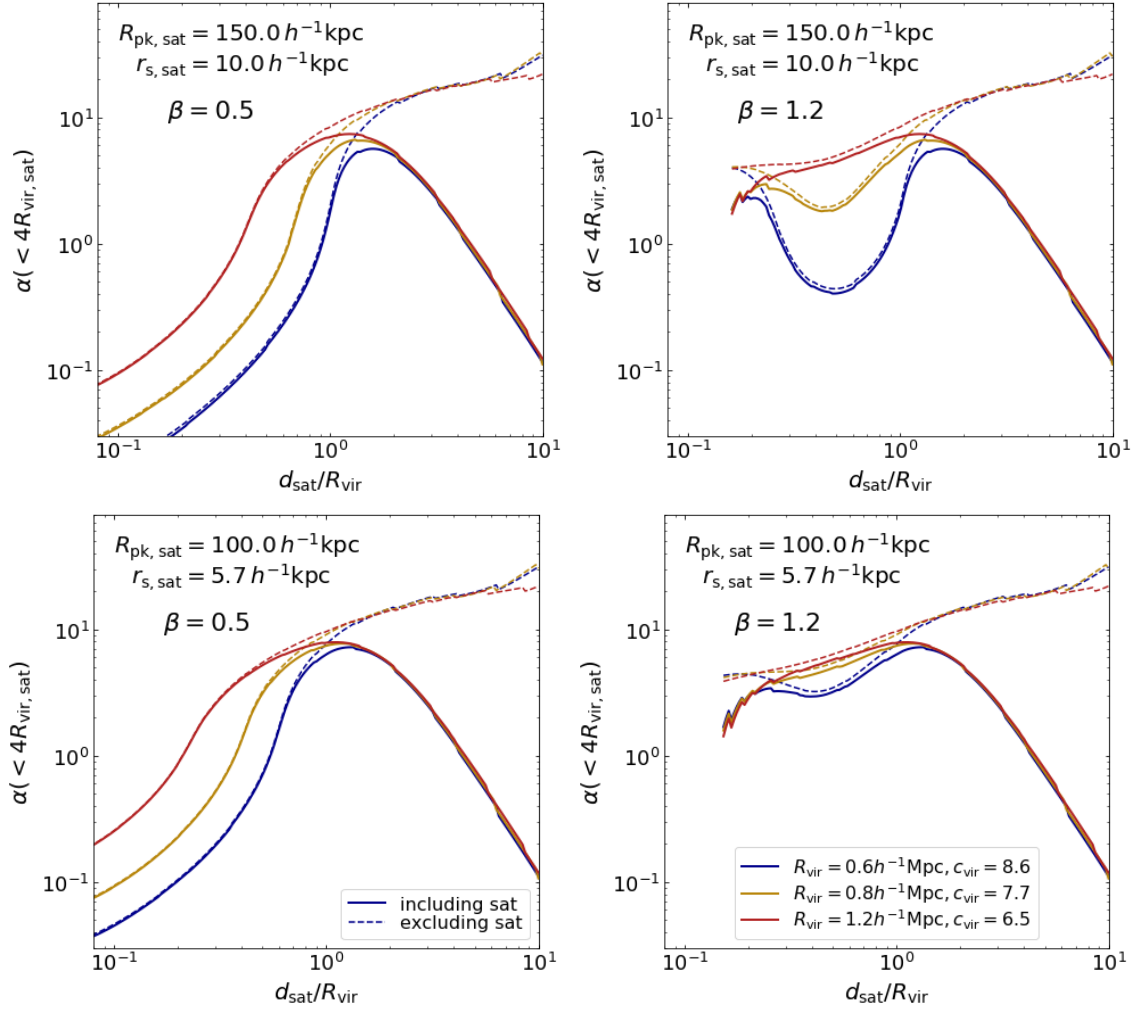


Figure 7. Tidal anisotropy $\alpha(< 4R_{\text{vir,sat}})$ centred on a satellite of current radius $R_{\text{vir,sat}}$ at distance d_{sat} from the centre of its spherical NFW host of radius R_{vir} and concentration c_{vir} . See Figure 5 for an illustration. Curves of different colours represent different combinations of R_{vir} and c_{vir} (with R_{vir} increasing from bottom to top around $d_{\text{sat}} \sim R_{\text{vir}}/2$ in all panels). Solid curves show results including the satellite profile which is modelled as a spherical NFW of radius $R_{\text{pk,sat}}$ and scale radius $r_{\text{s,sat}}$ (or concentration $c_{\text{pk,sat}} = R_{\text{pk,sat}}/r_{\text{s,sat}}$) as indicated, and truncated at the current radius $R_{\text{vir,sat}}$ as described in the text. *Upper and lower panels* show results for two choices of combinations of $R_{\text{pk,sat}}$ and $r_{\text{s,sat}}$, as indicated in the plot labels. $R_{\text{vir,sat}}$ is calculated using a toy model of mass loss (equation 63) with $\beta = 0.5$ in the *left panels* and $\beta = 1.2$ in the *right panels*. Dashed curves show results excluding the satellite profile (i.e., assuming the satellite contributes negligible density). All curves truncate at small distances where $R_{\text{vir,sat}} < r_{\text{s,sat}}$.

different smoothing scales $R_{\text{smooth}} = 4R_{\text{sat, vir}}$ at different d_{sat} and for different model parameters. Larger values of $\lambda \equiv R_{\text{smooth}}/R_{\text{vir}}$ at the same $d_{\text{sat}}/R_{\text{vir}}$ produce a lower anisotropy, which is sensible (in the limit $\lambda \gg d_{\text{sat}}/R_{\text{vir}}$, the anisotropy should become negligible). Indeed, the strongest decrease is seen in the *top left* panel (larger $R_{\text{pk,sat}}$, weaker mass loss rate) for the smallest host size (blue curves), all of which conspire to produce the largest λ at fixed $d_{\text{sat}}/R_{\text{vir}} \lesssim 1$. As the host size increases (red and yellow curves in same panel), or as the initial satellite radius decreases (bottom panels), or as the mass loss rate increases (right panels), α decreases by smaller amounts.

For a fixed host size, the $\beta = 1.2$ model shows a minimum in α for the smaller host sizes. The fact that α increases as the separation decreases below $d_{\text{sat}} \lesssim R_{\text{vir}}/2$ in all but the largest hosts, can be understood as an interplay of two effects: the smoothing radius is decreasing and the smoothing centre

is moving closer to the centre of symmetry. The latter effect is initially dominant (at $d_{\text{sat}} \lesssim R_{\text{vir}}$ where λ is large). At smaller d_{sat} , the decrease in λ becomes more rapid (equation 63), so that moving closer to the symmetry centre plays a weaker role than the fact that the anisotropic tidal field is being smoothed by a lesser amount. This leads to a rise in α beyond the point where these effects balance. The effect is not seen in the $\beta = 0.5$ cases over the range of scales plotted, consistent with the weaker mass loss in this model. Since $d_{\text{sat}} \rightarrow 0$ would bring us exactly to the symmetry centre, α is expected to *decrease* again in the $\beta = 1.2$ case for smaller d_{sat} (provided the smoothing radius remains non-zero), even when ignoring the satellite self-contribution. Indeed, there are indications of a maximum in α in the curves excluding the satellite, which coincidentally occur just before $R_{\text{vir,sat}}$ becomes smaller than $r_{\text{s,sat}}$.

Finally, the combined result of all these effects is to

produce an *overall maximum* in $\alpha(< 4R_{\text{vir,sat}})$ at $d_{\text{sat}} \gtrsim R_{\text{vir}}$ just outside the host, with maximum values between 5-8. This is in sharp contrast to the statistics of subhaloes seen in cosmological simulations which show typical values of $\alpha(< 4R_{\text{sat,vir}}) \lesssim 1.0$ (Zjupa et al. 2020). This is almost certainly a consequence of the fact that most satellites identified in a given simulation snapshot are *not* close to their first infall; satellites found further inside their host are indeed predicted to have smaller α in our models.

This suggests a further interesting application of our formalism. For a satellite population with some typical mass ratio $\mu_{\text{sat}} \sim (R_{\text{vir,sat}}/R_{\text{sat}})^3$ and typical separation $d_{\text{sat}}/R_{\text{vir}}$, measurements of $\alpha(< 4R_{\text{vir,sat}})$ in simulations could in principle be used to constrain empirical models of mass loss by comparing with plots such as Figure 7. This is an exercise we will pursue in future work.

4.3 Anisotropic halo

As our final example, we consider the tidal field of an axisymmetric halo. Simulated haloes are well-known to be triaxial (see, e.g. Allgood et al. 2006), with shapes that correlate with their large-scale environment (Faltenbacher & White 2010). The triaxiality of haloes is also known to be well-described using anisotropically scaled NFW profiles (Jing & Suto 2002). It is therefore interesting to explore the tidal influence of the anisotropic halo shape.

However, any such model involving smoothing at scales larger than the virial radius must account for the tidal influence of the halo *environment* as well, as we approximated in each of the models above. For the situation we are now interested in, we would need to also model genuine 2-halo effects due to large-scale structure (Pápai & Sheth 2013).⁵ A model focusing only on the halo profile, on its own, cannot provide realistic insight into the behaviour of the halo-centric $\alpha(< 4R_{\text{vir}})$. In the interest of completeness, however, we will show the results for the 1-halo contribution of such a model, leaving a fuller exploration of effects beyond the halo radius to future work.

With these caveats in mind, consider an axisymmetric halo profile given by

$$\begin{aligned} \Delta(\mathbf{r}) &= \Delta_{\text{NFW}} \left(\sqrt{z^2 + (x^2 + y^2)/b^2} |R_{\text{vir}}, c_{\text{vir}} \right) \\ &= \Delta_{\text{NFW}} \left(\frac{r}{b} \sqrt{1 - (1 - b^2)\mu^2} |R_{\text{vir}}, c_{\text{vir}} \right), \end{aligned} \quad (64)$$

where $0 < b \leq 1$ is the common value of the intermediate-to-major and minor-to-major eigenvalue ratios of the halo moment-of-inertia tensor (with $b = 1$ describing a spherical halo) and we aligned the major axis with the Cartesian z -axis.

The resulting calculation is in fact very similar to the one in section 4.1, since the anisotropy in the density has a similar (but not the same) structure as the filamentary profile studied there. Applying the Gaussian mixture (40), the

⁵ We can always consider an axisymmetric halo at the axis of and perfectly aligned with a filament. The resulting tidal anisotropy would be a straightforward combination of the results of this section and those of section 4.1. Apart from this somewhat contrived example, modelling the intermediate-scale environment of an anisotropic halo is more challenging.

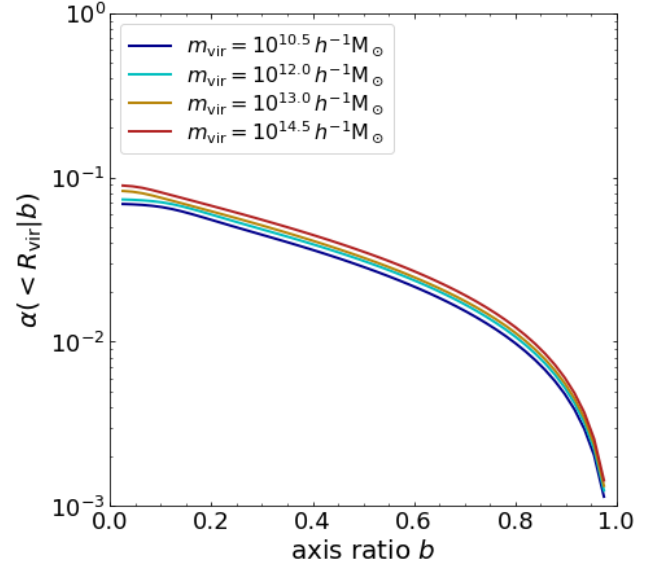


Figure 8. Halo-scale tidal anisotropy $\alpha(< R_{\text{vir}})$ for an axisymmetric NFW halo with profile (64), as a function of axis ratio b for a range of values of virial mass m_{vir} (coloured curves, decreasing in m_{vir} from bottom to top). We see a sharp increase in α as b decreases from unity and the haloes become aspherical, followed by a slower increase to a finite value as $b \rightarrow 0$. The anisotropy depends only weakly on halo mass.

$\ell = 0, 2$ multipole moments (equation 23) of each individual Gaussian component can be written as

$$\begin{aligned} \Delta_{00}(r|\sigma_j, r_s) &= \sqrt{4\pi} \left(\Delta_G(r|\sigma_j, r_s) \frac{\mathcal{D}(\kappa_j)}{\kappa_j} - 1 \right), \\ \Delta_{20}(r|\sigma_j, r_s) &= \sqrt{5\pi} \Delta_G(r|\sigma_j, r_s) \\ &\quad \times \left[\frac{3}{2\kappa_j^2} - \frac{\mathcal{D}(\kappa_j)}{\kappa_j} \left(1 + \frac{3}{2\kappa_j^2} \right) \right], \end{aligned} \quad (65)$$

where $\Delta_G(r|\sigma_j, r_s)$ was defined in equation (41), Dawson's integral $\mathcal{D}(z)$ was defined in equation (50) and we defined

$$\kappa_j(r) \equiv \frac{\sqrt{1-b^2}}{\sqrt{2}b} \left(\frac{r}{r_s \sigma_j} \right). \quad (66)$$

Equations (65) can be integrated (see equations 26 and 27) to give the single-component contributions to $\langle \Delta \rangle(< R)$ and $t(< R)$:

$$\begin{aligned} \langle \Delta \rangle(< R|\sigma_j, r_s) &= 3\Delta_j b^2 \left(\frac{r_s \sigma_j}{R} \right)^3 \left[\sqrt{\frac{\pi}{2}} \operatorname{erf} \left(\frac{R}{\sqrt{2} r_s \sigma_j} \right) \right. \\ &\quad \left. - \frac{\sqrt{2}b}{\sqrt{1-b^2}} e^{-R^2/(2r_s^2 \sigma_j^2)} \mathcal{D}(\kappa_j(R)) \right] \\ t(< R|\sigma_j, r_s) &= \frac{3\Delta_j}{2} \int_{\kappa_j(R)}^{\infty} \frac{ds}{s^2} e^{-b^2 s^2/(1-b^2)} \left[\frac{1}{s} - \left(\frac{2}{3} + \frac{1}{s^2} \right) \mathcal{D}(s) \right]. \end{aligned} \quad (67)$$

The integral defining $t(< R|\sigma_j, r_s)$ must be performed numerically in this case, but is straightforward to compute.

Figure 8 shows the resulting total $\alpha(< R_{\text{vir}})$ (note the smoothing scale) for a few halo masses m_{vir} as a function

of axisymmetry parameter b . We see little dependence on m_{vir} for all b . At fixed m_{vir} , on the other hand, $\alpha(< R_{\text{vir}})$ sharply increases as b decreases from unity and approaches a value $\lesssim 0.1$ as $b \rightarrow 0$. The trend as $b \rightarrow 1$ is sensible, since the anisotropy must vanish for a perfectly spherical halo. As we mentioned above, however, it is difficult to draw substantial further insight from this model due to the lack of environmental contributions to α .

5 SUMMARY & CONCLUSION

Motivated by the need to understand the nature of the tidal field of different cosmic web environments, in this work we have presented a descriptive analytical framework for studying the primary tool of interest, namely, the halo-centric tidal tensor spherically averaged on a smoothing scale proportional to the halo virial radius R_{vir} . Specifically, we were interested in studying the ‘tidal anisotropy’ scalar $\alpha(< 4R_{\text{vir}})$ (equation 6) in different cosmic web environments.

Although the formalism we developed in section 2 and Appendix A is capable of describing arbitrarily anisotropic tidal environments, we focused on axisymmetric anisotropies in this work, with the intent of building the simplest possible examples capable of providing insight into the behaviour of $\alpha(< 4R_{\text{vir}})$. Equations (26), (27) and (29), valid for any axisymmetric density distribution (22), form the core result of this work.

As a simple application of this formalism, we proved in general that any misalignment between the spherically averaged versions of the tidal tensor (1) and density Hessian (30) *must be a consequence of departures from axisymmetry in the unsmoothed density*. In other words, the misalignment angle between these two *smoothed* tensors can be thought of as a direct measurement of triaxiality of the *unsmoothed* field. This is an interesting example of a situation where smoothing with a spherical filter does not erase anisotropic information.

As examples of interesting cosmological situations, we studied three toy models (section 4):

- a spherical halo at the axis of a cylindrical filament,
- an off-centred satellite in a spherical host halo, and
- a halo with an axisymmetric density profile,

each of which results in a single special direction that serves as the axis of symmetry (see Figures 3 and 5).

In each of these cases, we used the spherical NFW profile (equation 36) as a building block to describe halo density profiles and satellite environments. Despite its simplicity, the NFW profile typically does not admit closed form expressions for the integrals defining the spherically averaged tidal tensor components, even for the restricted axisymmetric case. *A key simplification occurs by approximating the NFW profile itself as a mixture of spherical Gaussians* (section 3, equation 40). Although this converts a 2-parameter function into a sum of multiple (~ 20) Gaussian components, the resulting ability to analytically calculate $\alpha(< 4R_{\text{vir}})$ for each of our examples is, we believe, worth the additional complexity. We used standard numerical libraries to implement a non-negative least squares fit of the Gaussian mixture to the NFW profile (Figures 1 and 2), which was then propagated into the formalism for the tidal tensor.

The Gaussian mixture lends itself to considerable flexibility, as we showed in our toy models. For example, in the case of the halo in a filament (section 4.1), in addition to the halo’s NFW profile, the *filament’s* density profile can also be modelled as a Gaussian mixture (we used only one component for illustration). We showed that the resulting tidal tensor has a remarkably simple, closed form analytical structure (equation 56) such that $\alpha^{(\text{fil})}(< R) = 1/2$ when ignoring the halo’s self-contribution, for any smoothing scale. While the more realistic calculation including the halo contribution changes this to the behaviour seen in Figure 4, we argued that our calculation provides the first analytical insight into the observed fact that filamentary haloes in simulations are bounded by $\alpha(< 4R_{\text{vir}}) \gtrsim 0.5$ (see, e.g., Figure 7 of Paranjape et al. 2018).

For the satellite of radius $R_{\text{vir,sat}}$ off-centred from its host (section 4.2), the Gaussian mixture describing the satellite allowed us to easily approximate mass loss due to various dynamical mechanisms by simply discarding the Gaussian components in the satellite’s outskirts (illustrated in Figure 6). What constitutes the outskirts is decided by the specific model of mass loss; we argued that our formalism can be adapted in a straightforward manner to constrain such models by comparing predictions such as those in Figure 7 with measurements of $\alpha(< 4R_{\text{vir,sat}})$ in simulations. The simplified mass-loss models we explored also generically predict that $\alpha(< 4R_{\text{vir,sat}})$ has its maximum close to first infall, which should be possible to test in simulations.

Finally, we included the example of the axisymmetric halo for completeness (section 4.3, Figure 8), noting that a fuller understanding of $\alpha(< 4R_{\text{vir}})$ for such objects would require the inclusion of models of their external cosmic environment (e.g., along the lines described by Pápai & Sheth 2013).

Our formalism and associated models allow for several immediate applications and extensions, apart from those mentioned above. We conclude by discussing some of these here.

- Although the configurations we studied focused on filaments and substructure, haloes in voids are interesting too (e.g., Rieder et al. 2013), and can be easily described by our axisymmetric formalism similarly to our off-centred satellite example.

- For haloes in filaments, as we argued in section 4.1, a systematic study in N -body simulations of $\alpha(< 4R_{\text{vir}})$ as a function of distance from the filament axis would further help clarify the significance of the value $\alpha(< 4R_{\text{vir}}) = 1/2$ for such objects (see, e.g., Platen et al. 2008, who show that dynamical effects due to tidal fields can occur over distances of several tens of Mpc). Moreover, the near-universality of $\alpha(< 4R_{\text{vir}})$ with filament size seen in Figure 4 (if it persists for a broader population than perfectly on-axis haloes) might be useful in constraining filamentary profile shapes in simulations, using only measurements of halo-centric $\alpha(< 4R_{\text{vir}})$.

- There has also been considerable discussion in the literature as to which variables defined at which smoothing scales are the most suitable indicators of halo properties and large-scale correlations, with the fixed-scale overdensity $\langle \Delta \rangle (< R)$ with $R \simeq 1.2h^{-1}\text{Mpc}$ and halo-scaled tidal anisotropy $\alpha(< 4R_{\text{vir}})$ being primary contenders (Yan et al. 2013; Han et al. 2019; Goh et al. 2019; Ramakrishnan et al.

2019). Our analytical formalism would be a useful tool in disentangling some of these correlations, e.g., by studying $\alpha(< R)$ as a function of $\langle \Delta \rangle (< R)$ for different choices of R and in different cosmic web environments.

• Finally, an extension of the formalism to include anisotropies beyond axisymmetry would allow us to study more realistic (sub)halo configurations such as off-axis haloes in a filament, off-centred satellites in an aspherical host, aspherical haloes in a void, etc. This extension is tedious, but feasible (see the discussion at the end of Appendix A4). The associated Gaussian mixtures description of halo profiles with substructure would also have potential applications in semi-analytic modelling for gravitational lensing studies, galaxy cluster modelling, etc.

We will return to these problems in future studies.

ACKNOWLEDGMENTS

It is a pleasure to thank Ravi Sheth and Oliver Hahn for many insightful discussions, and the anonymous referee for a constructive report. This research is supported by the Associateship Scheme of ICTP, Trieste and the Ramanujan Fellowship awarded by the Department of Science and Technology, Government of India. This work used the open source computing packages NumPy (Van Der Walt et al. 2011)⁶, SciPy (Virtanen et al. 2020), Matplotlib (Hunter 2007)⁷ and Jupyter⁸ Notebook.

DATA AVAILABILITY

No new data were analysed in support of this research. Python code for producing the Gaussian mixtures and analytical models used in this work, along with a Jupyter notebook containing example calculations that reproduce all the main plots of the paper, can be downloaded from <https://bitbucket.org/aparanjape/gaussmixnfw>.

REFERENCES

- Abramowitz M., Stegun I. A., 1972, *Handbook of Mathematical Functions*. Dover Publications Inc., New York
- Allgood B., Flores R. A., Primack J. R., Kravtsov A. V., Wechsler R. H., Faltenbacher A., Bullock J. S., 2006, *MNRAS*, **367**, 1781
- Aragón-Calvo M. A., van de Weygaert R., Jones B. J. T., van der Hulst J. M., 2007, *ApJ*, **655**, L5
- Aragón-Calvo M. A., van de Weygaert R., Jones B. J. T., 2010, *MNRAS*, **408**, 2163
- Behroozi P. S., Wechsler R. H., Lu Y., Hahn O., Busha M. T., Klypin A., Primack J. R., 2014, *ApJ*, **787**, 156
- Binney J., Tremaine S., 1987, *Galactic dynamics*. Princeton University Press, Princeton, NJ
- Bond J. R., Myers S. T., 1996a, *ApJS*, **103**, 1
- Bond J. R., Myers S. T., 1996b, *ApJS*, **103**, 41
- Bond J. R., Myers S. T., 1996c, *ApJS*, **103**, 63
- Bond J. R., Kofman L., Pogosyan D., 1996, *Nature*, **380**, 603

- Borzyszkowski M., Porciani C., Romano-Díaz E., Garaldi E., 2017, *MNRAS*, **469**, 594
- Bullock J. S., Kolatt T. S., Sigad Y., Somerville R. S., Kravtsov A. V., Klypin A. A., Primack J. R., Dekel A., 2001, *MNRAS*, **321**, 559
- Burkert A., 1995, *ApJ*, **447**, L25
- Castorina E., Paranjape A., Hahn O., Sheth R. K., 2016, preprint, ([arXiv:1611.03619](https://arxiv.org/abs/1611.03619))
- Cautun M., van de Weygaert R., Jones B. J. T., 2013, *MNRAS*, **429**, 1286
- Cautun M., van de Weygaert R., Jones B. J. T., Frenk C. S., 2014, *MNRAS*, **441**, 2923
- Chisari N., et al., 2015, *MNRAS*, **454**, 2736
- Codis S., Pichon C., Devriendt J., Slyz A., Pogosyan D., Dubois Y., Sousbie T., 2012, *MNRAS*, **427**, 3320
- Cooray A., Sheth R., 2002, *Phys. Rep.*, **372**, 1
- Desjacques V., 2008, *MNRAS*, **388**, 638
- Desjacques V., Jeong D., Schmidt F., 2018, *J. Cosmology Astropart. Phys.*, **2018**, 017
- Diemer B., Kravtsov A. V., 2015, *ApJ*, **799**, 108
- Doroshkevich A. G., 1970, *Astrophysics*, **6**, 320
- Einasto J., 1965, *Trudy Astrofizicheskogo Instituta Alma-Ata*, **5**, 87
- Eisenstein D. J., Loeb A., 1995, *ApJ*, **439**, 520
- Faltenbacher A., White S. D. M., 2010, *ApJ*, **708**, 469
- Fard M. A., Taamoli S., Baghran S., 2019, *MNRAS*, **489**, 900
- Forero-Romero J. E., Hoffman Y., Gottlöber S., Klypin A., Yepes G., 2009, *MNRAS*, **396**, 1815
- Gao L., Springel V., White S. D. M., 2005, *MNRAS*, **363**, L66
- Goh T., et al., 2019, *MNRAS*, **483**, 2101
- Green S. B., van den Bosch F. C., 2019, *MNRAS*, **490**, 2091
- Hahn O., Porciani C., Carollo C. M., Dekel A., 2007a, *MNRAS*, **375**, 489
- Hahn O., Carollo C. M., Porciani C., Dekel A., 2007b, *MNRAS*, **381**, 41
- Hahn O., Porciani C., Dekel A., Carollo C. M., 2009, *MNRAS*, **398**, 1742
- Han J., Li Y., Jing Y., Nishimichi T., Wang W., Jiang C., 2019, *MNRAS*, **482**, 1900
- Hearin A. P., Behroozi P. S., van den Bosch F. C., 2016, *MNRAS*, **461**, 2135
- Hoffman Y., 1986, *ApJ*, **308**, 493
- Hoyle F., 1951, in *Problems of Cosmical Aerodynamics*. p. 195
- Hunter J. D., 2007, *Computing In Science & Engineering*, **9**, 90
- Icke V., 1973, *A&A*, **27**, 1
- Jing Y. P., Suto Y., 2002, *ApJ*, **574**, 538
- Jing Y. P., Suto Y., Mo H. J., 2007, *ApJ*, **657**, 664
- Jones B., van de Weygaert R., 2009, *Astrophysics and Space Science Proceedings*, **8**, 467
- Kraljic K., et al., 2019, *MNRAS*, **483**, 3227
- Lawson C. L., Hanson R. J., 1995, *Solving least squares problems*, [rev. ed.] edn. Philadelphia : SIAM, <http://www.loc.gov/catdir/enhancements/fy0617/95035178-t.html>
- Lee J., Pen U.-L., 2000, *ApJ*, **532**, L5
- Libeskind N. I., et al., 2018, *MNRAS*, **473**, 1195
- Monaco P., 1999, in Giuricin G., Mezzetti M., Salucci P., eds, *Astronomical Society of the Pacific Conference Series Vol. 176, Observational Cosmology: The Development of Galaxy Systems*. p. 186
- Musso M., Cadiou C., Pichon C., Codis S., Kraljic K., Dubois Y., 2018, *MNRAS*, **476**, 4877
- Navarro J. F., Frenk C. S., White S. D. M., 1996, *ApJ*, **462**, 563
- Navarro J. F., Frenk C. S., White S. D. M., 1997, *ApJ*, **490**, 493
- Navarro J. F., et al., 2004, *MNRAS*, **349**, 1039
- Ogiya G., van den Bosch F. C., Hahn O., Green S. B., Miller T. B., Burkert A., 2019, *MNRAS*, **485**, 189
- Pápai P., Sheth R. K., 2013, *MNRAS*, **429**, 1133
- Paranjape A., Hahn O., Sheth R. K., 2018, *MNRAS*, **476**, 3631

⁶ <http://www.numpy.org>

⁷ <https://matplotlib.org/>

⁸ <https://jupyter.org>

- Peebles P. J. E., 1969, *ApJ*, **155**, 393
- Platen E., van de Weygaert R., Jones B. J. T., 2008, *MNRAS*, **387**, 128
- Porciani C., Dekel A., Hoffman Y., 2002a, *MNRAS*, **332**, 339
- Porciani C., Dekel A., Hoffman Y., 2002b, *MNRAS*, **332**, 325
- Ramakrishnan S., Paranjape A., Hahn O., Sheth R. K., 2019, *MNRAS*, **489**, 2977
- Rieder S., van de Weygaert R., Cautun M., Beygu B., Portegies Zwart S., 2013, *MNRAS*, **435**, 222
- Rossi G., 2012, *MNRAS*, **421**, 296
- Schäfer B. M., 2009, *International Journal of Modern Physics D*, **18**, 173
- Shandarin S. F., Zeldovich Y. B., 1989, *Reviews of Modern Physics*, **61**, 185
- Shen J., Abel T., Mo H. J., Sheth R. K., 2006, *ApJ*, **645**, 783
- Sheth R. K., Tormen G., 2004, *MNRAS*, **350**, 1385
- Sheth R. K., Mo H. J., Tormen G., 2001a, *MNRAS*, **323**, 1
- Sheth R. K., Hui L., Diaferio A., Scoccimarro R., 2001b, *MNRAS*, **325**, 1288
- Sousbie T., 2011, *MNRAS*, **414**, 350
- Van Der Walt S., Colbert S. C., Varoquaux G., 2011, preprint, ([arXiv:1102.1523](https://arxiv.org/abs/1102.1523))
- Virtanen P., et al., 2020, *Nature Methods*, **17**, 261
- Wechsler R. H., Bullock J. S., Primack J. R., Kravtsov A. V., Dekel A., 2002, *ApJ*, **568**, 52
- White S. D. M., 1984, *ApJ*, **286**, 38
- White S. D. M., Silk J., 1979, *ApJ*, **231**, 1
- Yan H., Fan Z., White S. D. M., 2013, *MNRAS*, **430**, 3432
- Zel'dovich Y. B., 1970, *A&A*, **5**, 84
- Zjupa J., Paranjape A., Hahn O., Pakmor R., 2020, arXiv e-prints, p. [arXiv:2009.03329](https://arxiv.org/abs/2009.03329)
- van Haarlem M., van de Weygaert R., 1993, *ApJ*, **418**, 544
- van de Weygaert R., Babul A., 1993, *JRASC*, **87**, 213
- van de Weygaert R., Bertschinger E., 1996, *MNRAS*, **281**, 84
- van de Weygaert R., Bond J. R., 2008, *Observations and Morphology of the Cosmic Web*. Springer, Heidelberg, p. 24, doi:10.1007/978-1-4020-6941-3_11
- van den Bosch F. C., Ogiya G., 2018, *MNRAS*, **475**, 4066
- van den Bosch F. C., Tormen G., Giocoli C., 2005, *MNRAS*, **359**, 1029

APPENDIX A: DETAILS OF CALCULATIONS

In this Appendix we build up the analytical formalism used in the text to calculate the spherically averaged tidal tensor and the scalar tidal anisotropy $\alpha(< R)$.

A1 Tidal tensor in polar coordinates

We will use the usual spherical polar coordinates $\{r, \theta, \phi\}$ related to Cartesian coordinates $\{x, y, z\}$ through

$$x = r s_\theta c_\phi \quad ; \quad y = r s_\theta s_\phi \quad ; \quad z = r c_\theta \quad (\text{A1})$$

As in the main text, we abbreviate $\sin(\theta) = s_\theta$ and $\cos(\theta) = c_\theta$ for any angle θ . We will also use the local rotation relating the unit vectors in the Cartesian and spherical polar bases (Binney & Tremaine 1987)

$$\begin{aligned} \hat{r} &= s_\theta (c_\phi \hat{x} + s_\phi \hat{y}) + c_\theta \hat{z} \\ \hat{\theta} &= c_\theta (c_\phi \hat{x} + s_\phi \hat{y}) - s_\theta \hat{z} \\ \hat{\phi} &= -s_\phi \hat{x} + c_\phi \hat{y}, \end{aligned} \quad (\text{A2})$$

which can be summarised as

$$\mathbf{e}_\alpha = R_\alpha^i \mathbf{e}_i \quad ; \quad \mathbf{e}_i = R_\alpha^i \mathbf{e}_\alpha, \quad (\text{A3})$$

where repeated indices are summed, with $\alpha = \{r, \theta, \phi\}$ and $i = \{x, y, z\}$, and where the local rotation matrix R_α^i is given by

$$R_\alpha^i = \begin{pmatrix} s_\theta c_\phi & s_\theta s_\phi & c_\theta \\ c_\theta c_\phi & c_\theta s_\phi & -s_\theta \\ -s_\phi & c_\phi & 0 \end{pmatrix}, \quad (\text{A4})$$

with the inverse given by $R_\alpha^i = (R_\alpha^i)^{-1} = (R_\alpha^i)^T$ (our convention is that the upper index is the column index and the lower index is the row index).

For any vector $\mathbf{v} = v_i \mathbf{e}_i = v_\alpha \mathbf{e}_\alpha$, the transformations relating the Cartesian components $\{v_i\}$ and the spherical components $\{v_\alpha\}$ are

$$v_i = R_\alpha^i v_\alpha \quad ; \quad v_\alpha = R_\alpha^i v_i. \quad (\text{A5})$$

Similarly, for any symmetric tensor $T = T_{ij} (\mathbf{e}_i \otimes \mathbf{e}_j) = T_{\alpha\beta} (\mathbf{e}_\alpha \otimes \mathbf{e}_\beta)$, we have

$$T_{ij} = R_\alpha^i R_\beta^j T_{\alpha\beta} \quad ; \quad T_{\alpha\beta} = R_\alpha^i R_\beta^j T_{ij}. \quad (\text{A6})$$

Explicitly, we have

$$\begin{aligned} T_{xx} &= c_\phi^2 A_+ + s_\phi^2 T_{\phi\phi} - s_{2\phi} B_+ \\ T_{yy} &= s_\phi^2 A_+ + c_\phi^2 T_{\phi\phi} + s_{2\phi} B_+ \\ T_{zz} &= A_- \\ T_{xy} &= \frac{1}{2} s_{2\phi} (A_+ - T_{\phi\phi}) + c_{2\phi} B_+ \\ T_{xz} &= c_\phi C - s_\phi B_- \\ T_{yz} &= s_\phi C + c_\phi B_-, \end{aligned} \quad (\text{A7})$$

where we defined the quantities

$$\begin{aligned} A_+ &\equiv s_\theta^2 T_{rr} + c_\theta^2 T_{\theta\theta} + s_{2\theta} T_{r\theta} \\ A_- &\equiv c_\theta^2 T_{rr} + s_\theta^2 T_{\theta\theta} - s_{2\theta} T_{r\theta} \\ B_+ &\equiv s_\theta T_{r\phi} + c_\theta T_{\theta\phi} \\ B_- &\equiv c_\theta T_{r\phi} - s_\theta T_{\theta\phi} \\ C &\equiv \frac{1}{2} s_{2\theta} (T_{rr} - T_{\theta\theta}) + c_{2\theta} T_{r\theta}. \end{aligned} \quad (\text{A8})$$

As a check, a direct calculation shows that the linear and quadratic rotational invariants I_1 and I_2 obey the identities

$$\begin{aligned} I_1 &= T_{xx} + T_{yy} + T_{zz} = T_{rr} + T_{\theta\theta} + T_{\phi\phi} \\ I_2 &= T_{xx} T_{yy} - T_{xy}^2 + T_{xx} T_{zz} - T_{xz}^2 + T_{yy} T_{zz} - T_{yz}^2 \\ &= T_{rr} T_{\theta\theta} - T_{r\theta}^2 + T_{rr} T_{\phi\phi} - T_{r\phi}^2 + T_{\theta\theta} T_{\phi\phi} - T_{\theta\phi}^2, \end{aligned} \quad (\text{A9})$$

as expected from the fact that equations (A2) constitute a rotation of basis vectors. Note that $q^2 = I_1^2 - 3I_2$ (equation 7). These expressions will be useful in building $\alpha(< R)$ later.

Consider the tidal tensor T defined in equation (1). The spherical polar components $T_{\alpha\beta}$ can be expressed in terms of spherical polar derivatives of ψ using equation (8) and the derivative identities

$$\begin{aligned} \partial_\theta \hat{r} &= \hat{\theta} \quad ; \quad \partial_\phi \hat{\theta} = -\hat{r} \quad ; \quad \partial_\phi \hat{\phi} = -\left(s_\theta \hat{r} + c_\theta \hat{\theta}\right) \\ \partial_\phi \hat{r} &= s_\theta \hat{\phi} \quad ; \quad \partial_\phi \hat{\theta} = c_\theta \hat{\phi}, \end{aligned} \quad (\text{A10})$$

with all other derivatives of the polar unit vectors being zero. This leads to equation (9). As a check, note that the trace of the tensor recovers the Laplacian of the potential in polar

coordinates:

$$T_{rr} + T_{\theta\theta} + T_{\phi\phi} \quad (\text{A11})$$

$$\begin{aligned} &= \partial_r^2 \psi + \frac{2}{r} \partial_r \psi + \frac{1}{r^2} \left[\partial_\theta^2 \psi + \frac{c_\theta}{s_\theta} \partial_\theta \psi + \frac{1}{s_\theta^2} \partial_\phi^2 \psi \right] \\ &= \frac{1}{r^2} \partial_r (r^2 \partial_r \psi) + \frac{1}{r^2} \left[\frac{1}{s_\theta} \partial_\theta (s_\theta \partial_\theta \psi) + \frac{1}{s_\theta^2} \partial_\phi^2 \psi \right] \\ &= \nabla^2 \psi. \end{aligned} \quad (\text{A12})$$

A2 Multipole expansions

Here we collect some useful standard results concerning spherical harmonics and related functions. The spherical harmonics are given by

$$Y_\ell^m(\hat{r}) = N_{\ell m} P_\ell^m(\mu) e^{im\phi}, \quad (\text{A13})$$

with $i = \sqrt{-1}$ and $P_\ell^m(\mu)$ being the associated Legendre functions satisfying

$$P_\ell^m(\mu) = \frac{(-1)^m}{2^\ell \ell!} (1 - \mu^2)^{m/2} \frac{d^{\ell+m}}{d\mu^{\ell+m}} (\mu^2 - 1)^\ell, \quad (\text{A14})$$

and where $N_{\ell m}$ is a normalisation constant given by

$$N_{\ell m} = \sqrt{\frac{(2\ell+1)}{4\pi} \frac{(\ell-m)!}{(\ell+m)!}}. \quad (\text{A15})$$

The following identities are useful:

$$\begin{aligned} \frac{1}{s_\theta} \partial_\theta f &= -\partial_\mu f \\ \partial_\theta^2 f &= -\mu \partial_\mu f + (1 - \mu^2) \partial_\mu^2 f \\ (\mu^2 - 1) \partial_\mu P_\ell &= \ell (\mu P_\ell(\mu) - P_{\ell-1}(\mu)) \\ \partial_\theta^2 P_\ell &= -\ell(\ell+1) P_\ell + \mu \partial_\mu P_\ell \\ s_{2\theta} \partial_\theta P_\ell &= 2\ell \mu (\mu P_\ell - P_{\ell-1}), \end{aligned} \quad (\text{A16})$$

where f is any function of μ and $P_\ell(\mu) = P_\ell^{m=0}(\mu)$ (see equation A14) are Legendre polynomials satisfying the integral relations

$$\int_{-1}^1 \frac{d\mu}{2} P_\ell(\mu) = \delta_{\ell,0}, \quad (\text{A17})$$

$$\int_{-1}^1 \frac{d\mu}{2} P_\ell(\mu) P_{\ell'}(\mu) = \frac{1}{2\ell+1} \delta_{\ell,\ell'}, \quad (\text{A18})$$

where $\delta_{\ell,\ell'}$ is the Kronecker delta symbol.

A3 Azimuthal averaging

As discussed in section 2.3, the spherical average of any field can be thought of as two angular averages followed by a radial average. Here we compile the expressions for the first of the angular averages, namely over the azimuthal angle ϕ , for the tidal tensor (1).

Focusing on a single but generic harmonic coefficient

$\psi_{\ell m}(r)$ and using equation (A7) leads to

$$\begin{aligned} \langle T_{xx} \rangle_\phi &= \frac{1}{2} \delta_{m,0} (\tilde{A}_+ + \tilde{T}_{\phi\phi}) + \frac{1}{4} (\delta_{m,2} + \delta_{m,-2}) (\tilde{A}_+ - \tilde{T}_{\phi\phi}) \\ &\quad - \frac{i}{2} (\delta_{m,2} - \delta_{m,-2}) \tilde{B}_+ \\ \langle T_{yy} \rangle_\phi &= \frac{1}{2} \delta_{m,0} (\tilde{A}_+ + \tilde{T}_{\phi\phi}) - \frac{1}{4} (\delta_{m,2} + \delta_{m,-2}) (\tilde{A}_+ - \tilde{T}_{\phi\phi}) \\ &\quad + \frac{i}{2} (\delta_{m,2} - \delta_{m,-2}) \tilde{B}_+ \\ \langle T_{zz} \rangle_\phi &= \delta_{m,0} \tilde{A}_- \\ \langle T_{xy} \rangle_\phi &= \frac{i}{4} (\delta_{m,2} - \delta_{m,-2}) (\tilde{A}_+ - \tilde{T}_{\phi\phi}) + \frac{1}{2} (\delta_{m,2} + \delta_{m,-2}) \tilde{B}_+ \\ \langle T_{xz} \rangle_\phi &= \frac{1}{2} (\delta_{m,1} + \delta_{m,-1}) \tilde{C} - \frac{i}{2} (\delta_{m,1} - \delta_{m,-1}) \tilde{B}_- \\ \langle T_{yz} \rangle_\phi &= \frac{i}{2} (\delta_{m,1} - \delta_{m,-1}) \tilde{C} - \frac{1}{2} (\delta_{m,1} + \delta_{m,-1}) \tilde{B}_-, \end{aligned} \quad (\text{A19})$$

where $\tilde{A}_\pm, \tilde{B}_\pm, \tilde{C}$ and $\tilde{T}_{\phi\phi}$ are obtained by setting $\phi = 0$ in A_\pm, B_\pm, C (equation A8) and $T_{\phi\phi}$ (equation 9), respectively, and we used the identities

$$\begin{aligned} \langle c_{m'\phi} e^{im\phi} \rangle_\phi &= \frac{1}{2} (\delta_{m,m'} + \delta_{m,-m'}) \\ \langle s_{m'\phi} e^{im\phi} \rangle_\phi &= \frac{i}{2} (\delta_{m,m'} - \delta_{m,-m'}), \end{aligned} \quad (\text{A20})$$

where $m' \geq 0$.

A4 Axisymmetric model

For the reasons discussed in the main text, we focus attention on the axisymmetric case in which all multipoles with $m \neq 0$ vanish. This leads to

$$\begin{aligned} \langle T_{xx} \rangle_\Omega &= \frac{1}{2} \langle \tilde{A}_+ + \tilde{T}_{\phi\phi} \rangle_\mu = \langle T_{yy} \rangle_\Omega \\ \langle T_{zz} \rangle_\Omega &= \langle \tilde{A}_- \rangle_\mu, \end{aligned} \quad (\text{A21})$$

and the remaining angle-averaged components vanish, so that the angle-averaged tidal tensor is diagonal.

Using the identities in equation (A16) and suppressing the explicit dependence of $\psi_{\ell 0}$ and P_ℓ on r and μ , respectively, we find

$$\begin{aligned} N_{\ell 0}^{-1} \tilde{A}_- &= \psi_{\ell 0}'' \mu^2 P_\ell + \frac{1}{r} \psi_{\ell 0}' [P_\ell - (2\ell+1)\mu^2 P_\ell + 2\ell \mu P_{\ell-1}] \\ &\quad + \frac{1}{r^2} \psi_{\ell 0} [-\ell(\ell+1)P_\ell + \ell(\ell+2)\mu^2 P_\ell - \ell \mu P_{\ell-1}] \\ N_{\ell 0}^{-1} (\tilde{A}_+ + \tilde{T}_{\phi\phi}) &= \psi_{\ell 0}'' (1 - \mu^2) P_\ell + \frac{1}{r} \psi_{\ell 0}' [P_\ell + (2\ell+1)\mu^2 P_\ell - 2\ell \mu P_{\ell-1}] \\ &\quad + \frac{1}{r^2} \psi_{\ell 0} [-\ell(\ell+2)\mu^2 P_\ell + \ell \mu P_{\ell-1}] \end{aligned} \quad (\text{A22})$$

where a prime denotes a derivative with respect to r . As a check, note that

$$\begin{aligned} \tilde{A}_- + \tilde{A}_+ + \tilde{T}_{\phi\phi} &= N_{\ell 0} P_\ell(\mu) \left[\psi_{\ell 0}'' + \frac{2}{r} \psi_{\ell 0}' - \frac{1}{r^2} \ell(\ell+1) \psi_{\ell 0} \right] \\ &= \langle \nabla^2 (N_{\ell 0} \psi_{\ell 0} P_\ell) \rangle_\phi = \langle \nabla^2 \psi(\mathbf{r}) \rangle_\phi, \end{aligned} \quad (\text{A23})$$

which correctly recovers the azimuthally averaged trace of the tidal tensor.

To average equation (A22) over μ , we note that $P_1(\mu) = \mu$ and $P_2(\mu) = (3\mu^2 - 1)/2$, so that equations (A22) can be rewritten as

$$\begin{aligned} N_{\ell 0}^{-1} \tilde{A}_- &= \frac{1}{3} \psi''_{\ell 0} P_\ell (2P_2 + 1) \\ &+ \frac{1}{r} \psi'_{\ell 0} \left[P_\ell - \frac{1}{3} (2\ell + 1) P_\ell (2P_2 + 1) + 2\ell P_1 P_{\ell-1} \right] \\ &+ \frac{1}{r^2} \psi_{\ell 0} \left[-\ell(\ell + 1) P_\ell + \frac{1}{3} \ell(\ell + 2) P_\ell (2P_2 + 1) \right. \\ &\quad \left. - \ell P_1 P_{\ell-1} \right] \\ N_{\ell 0}^{-1} (\tilde{A}_+ + \tilde{T}_{\phi\phi}) &= -\frac{2}{3} \psi''_{\ell 0} P_\ell (P_2 - 1) \\ &+ \frac{1}{r} \psi'_{\ell 0} \left[P_\ell + \frac{1}{3} (2\ell + 1) P_\ell (2P_2 + 1) - 2\ell P_1 P_{\ell-1} \right] \\ &+ \frac{1}{r^2} \psi_{\ell 0} \left[-\frac{1}{3} \ell(\ell + 2) P_\ell (2P_2 + 1) + \ell P_1 P_{\ell-1} \right]. \quad (\text{A24}) \end{aligned}$$

Using the relations (A17) and (A18) then kills all multipoles except $\ell = 0$ and $\ell = 2$, and we have

$$\begin{aligned} \langle \tilde{A}_- \rangle_\mu &= \frac{N_{00}}{3} \delta_{\ell,0} \left(\psi''_{00} + \frac{2}{r} \psi'_{00} \right) \\ &+ \frac{2N_{20}}{15} \delta_{\ell,2} \left(\psi''_{20} + \frac{5}{r} \psi'_{20} + \frac{3}{r} \psi_{20} \right) \\ \langle \tilde{A}_+ + \tilde{T}_{\phi\phi} \rangle_\mu &= \frac{2N_{00}}{3} \delta_{\ell,0} \left(\psi''_{00} + \frac{2}{r} \psi'_{00} \right) \\ &- \frac{2N_{20}}{15} \delta_{\ell,2} \left(\psi''_{20} + \frac{5}{r} \psi'_{20} + \frac{3}{r} \psi_{20} \right). \quad (\text{A25}) \end{aligned}$$

Recognising $\langle \Delta \rangle_\Omega(r) - 1$ as given in equation (20) in the monopole term in equations (A25) and defining $t(r)$ using equation (21) then leads to equations (19).

Departing from $m = 0$ would mean accounting for $m = \pm 1, \pm 2$ terms in equations (A19), whose averages over μ and r would not only modify the diagonal terms in equation (24), but also introduce off-diagonal terms in general. The calculation of $q^2(< R)$ and hence $\alpha(< R)$ would then need to use equation (A9) in its full glory.

APPENDIX B: SETTING UP THE GAUSSIAN MIXTURE

In this Appendix, we describe our choices for the number of components N_c and the widths σ_j of each component ($1 \leq j \leq N_c$) for the Gaussian mixture approximation (40) to the NFW profile. In principle, one should optimise these quantities so as to produce the smallest possible error in Figure 2. In practice, we have found it easier to fix these numbers using the arguments described below, with a *post hoc* justification provided by the accuracy achieved in Figure 2. Our subsequent fits are performed using the non-negative least squares (NNLS) algorithm (Lawson & Hanson 1995) implemented in SciPy as `scipy.optimize.nnls`.

The guiding principle we adopt in fitting the NFW profile (36) is to sample the profile at values x_j of the dimensionless variable $x \equiv r/r_s$ where the logarithmic slope of the NFW profile matches the corresponding slope of a single Gaussian component of width σ_j . It is easy to show that this happens when

$$\sigma_j^2 = \frac{x_j^2(1+x_j)}{(1+3x_j)}. \quad (\text{B1})$$

We start by choosing the minimum and maximum values of x , respectively x_{\min} and x_{\max} . The maximum is conservatively set to $x_{\max} = 10 c_{\text{vir}}$. The minimum is also chosen to scale approximately linearly with concentration, with a mild additional dependence on R_{vir} and r_{force} (set by trial and error to ensure stability over a wide dynamic range) and a hard lower limit at $0.2 r_{\text{force}}/r_s$.

We then choose $N_c = 2n_c + 3$ components, with the integer n_c to be determined, such that three of the values $\{x_j\}$ are fixed as $x_1 = x_{\min}$, $x_{2n_c+3} = x_{\max}$ and $x_{n_c+2} = 1$. The remaining values then fan outwards symmetrically in n_c logarithmic intervals on either side from $x = 1$, giving a total of $2n_c + 3$ components. The logarithmic spacing and number of these intermediate components is chosen so as to give the maximum spread in samples while ensuring that the NNLS algorithm (implemented as below) converges. After some trial and error, for the number of components we settled on using $n_c \simeq 9$, with a weak dependence on R_{vir} and r_{force} and an upper limit of $n_c \leq 10$. We also choose to mildly cluster the components close to $x = 1$ where the NFW logarithmic slope is changing most rapidly.

The last piece to put in place is the summation constraint (42) for the weights, which we do as follows. Since there are N_c weights $\{w_j\}$ to be determined, the standard inversion problem (i.e., without imposing non-negativity of the weight) would be over-determined if we use all N_c of the NFW samples as well as the summation constraint. In order to keep the problem well-determined, we therefore start with $N_c - 1$ of the samples at $x = x_\beta$, $2 \leq \beta \leq N_c$ as the $(N_c - 1) \times 1$ column vector V_β , so that

$$V_\beta = \Delta_{\text{NFW}}(r_s x_\beta | R_{\text{vir}}, c_{\text{vir}}); \quad 2 \leq \beta \leq N_c. \quad (\text{B2})$$

We then define the $(N_c - 1) \times N_c$ matrix F using

$$F_{\beta j} = \Delta_G(r_s x_\beta | \sigma_j, r_s), \quad (\text{B3})$$

where $2 \leq \beta \leq N_c$, $1 \leq j \leq N_c$ and $\Delta_G(r | \sigma_j, r_s)$ was defined in equation (41), so that the corresponding $(N_c - 1)$ -dimensional subspace of the Gaussian mixture problem (40) can be written as the equation

$$F_{\beta j} W_j = V_\beta.$$

In the absence of the summation constraint, this under-determined problem can be solved using NNLS by minimising the Euclidean norm

$$\|F^T F W - F^T V\|$$

leading to an unconstrained least squares estimate of the full N_c -dimensional vector W . This is, of course, not what we want, since the summation constraint is not implemented and the solution would also have highly degenerate component weights due to the under-determined nature of the standard inversion problem.

Written like this, however, the summation constraint

is now straightforward to include. We simply augment the vector $F^T V$ with the value 1, and increase the dimension of the matrix $F^T F$ by one, adding a row and column with all elements except the last being unity. The Gaussian mixture equation (40) augmented by the summation constraint can then be summarised as minimising the norm

$$\|G\tilde{W} - S\|, \quad (\text{B4})$$

where the $(N_c + 1) \times (N_c + 1)$ matrix G is given by

$$G = \left(\begin{array}{ccc|c} & & & \vdots \\ & F^T F & & 1 \\ & & & \vdots \\ \hline \cdots & 1 & \cdots & 0 \end{array} \right), \quad (\text{B5})$$

the $(N_c + 1) \times 1$ vector S is

$$S = \left(\begin{array}{c} F^T V \\ \hline 1 \end{array} \right), \quad (\text{B6})$$

and the $(N_c + 1) \times 1$ vector \tilde{W} is

$$\tilde{W} = \left(\begin{array}{c} W \\ \hline \tilde{w} \end{array} \right), \quad (\text{B7})$$

with \tilde{w} being a Lagrange multiplier that enforces the summation constraint. We have used NNLS on equation (B4) to produce the results discussed in the main text.